Exploring Light's Interactions with Bubbles and Light Absorbers in Photoelectrochemical Devices using Ray Tracing

A Technical Report by

John Colby Stevens

The Joint Center for Artificial Photosynthesis,
Lawrence Berkeley National Laboratory

Department of Mechanical Engineering,
University of California, Berkeley

December 2012

DISCLAIMER

This document was prepared as an account of work sponsored by the United States Government. While this document is believed to contain correct information, neither the United States Government nor any agency thereof, nor The Regents of the University of California, nor any of their employees, makes any warranty, express or implied, or assumes any legal responsibility for the accuracy, completeness, or usefulness of any information, apparatus, product, or process disclosed, or represents that its use would not infringe privately owned rights. Reference herein to any specific commercial product, process, or service by its trade name, trademark, manufacturer, or otherwise, does not necessarily constitute or imply its endorsement, recommendation, or favoring by the United States Government or any agency thereof, or The Regents of the University of California. The views and opinions of authors expressed herein do not necessarily state or reflect those of the United States Government or any agency thereof or The Regents of the University of California. Ernest Orlando Lawrence Berkeley National Laboratory is an equal opportunity employer.

Abstract

Ray tracing was used to perform optical optimization of arrays of photovoltaic microrods and explore the interaction between light and bubbles of oxygen gas on the surface of the microrods. The incident angle of light was varied over a wide range. The percent of incident light absorbed by the microrods and reflected by the bubbles was computed over this range. It was found that, for the 10 μm diameter, 100 μm tall $SrTiO_3$ microrods simulated in the model, the optimal center-to-center spacing was 14 μm for a square grid. This geometry produced 75% average and 90% maximum absorbance. For a triangular grid using the same microrods, the optimal center-to-center spacing was 14 μm. This geometry produced 67% average and 85% maximum absorbance. For a randomly laid out grid of 5 μm diameter, 100 μm tall $SrTiO_3$ microrods with an average center-to-center spacing of 20 μm, the average absorption was 23% and the maximum absorption was 43%. For a 50% areal coverage fraction of bubbles on the absorber surface, between 2%-20% of the incident light energy was reflected away from the rods by the bubbles, depending upon incident angle and bubble morphology.

Keywords
Strontium Titanate, Photoelectrochemical Devices, Water Splitting, Solar Fuels Photovoltaic Energy, Microrod Array, Light Absorption, Optics, Ray Tracing, Genetic Algorithm, Bubbles, Joint Center for Artificial Photosynthesis (JCAP).

Contents

1. Introduction……6
2. Review of Photoelectrochemical Device Design and Chemistry……6
2.1 PEC Design……6
2.2 PEC Chemistry……7
2.3 Constraints on Photovoltaic Materials in a PEC……9
3. Microrod Array Structure and Advantages……10
3.1 Microrod Geometry Overview……10
3.2 Catalyst Considerations……10
3.3 Decoupling of Light Absorbance and Charge Transport……11
3.4 Light Trapping in Microrods……12
3.5 Intra-rod Light Scattering……13
3.6 Material Conservation Considerations……14
4. Theories in Optics Modeling……15
4.1 Physical Optics……15
4.2 Geometric Optics……16
5. Computational Scheme for Modeling Light Absorbance in Microrod Arrays……18
5.1 Ambient Environment……18
5.2 Thin Films……18
5.3 Modeling Ray Energy Absorbance from Reflections……20
5.4 Simulation of Microrod Geometry……21
5.5 Microrod Array Grid Generation……22
5.6 Setting and Tracking Ray Position as a Function of Time……22
5.7 Setting Initial Ray Propagation Direction……23
5.8 Modeling Reflection Locations From Ellipsoids……24
5.9 Simulation Exit Criteria……24
5.10 Overall Computational Scheme……26
5.11 Implementation of a Genetic Algorithm to Find Optimal Grid Geometries……26
6. Results of Microrod Absorbance Simulations……27
6.1 Ray Tracing Simulation Results For Regular Grids……27
6.2 Ray Tracing Simulation Results for Random Grids……29
6.3 Results from Other Investigators……31
7. Bubbles in a PEC Device……32
7.1 The Importance of Light Interactions with Bubbles in a PEC Device……32
7.2 The Physics of Bubbles……32
7.3 Methods for Modeling Light Interactions with Bubbles……34
8. Computational Scheme for Modeling Light Scattering by Oxygen Bubbles……35
8.1 Ambient Environment……35
8.2 Simulation of Bubble Geometry……35
8.3 Setting and Tracking Ray Position and Energy as a Function of Time……36
8.4 Setting Initial Ray Propagation Direction……36
8.5 Modeling Reflection Locations from Bubbles……37
8.6 Simulation Exit Criteria……37
8.7 Overall Computational Scheme……37

9. Results of Bubble Reflectance Simulations.....37
9.1 Results for $\theta_{contact}$=45°.....37
9.2 Results for $\theta_{contact}$=135°.....39
10. Future Modeling and Experimental Work.....41
10.1 Advantages of using a Maxwell Equation Solving Optical Model that Simulates Microrods.....41
10.2 Experimentally Measuring Bubble Reflectance.....42
10.3 Add Bubbles in Other Locations.....42
10.4 Incorporate the Effects of Temperature Rise into the Model.....42
11. Conclusion.....42
12. Acknowledgments.....42
13. References.....43

1. Introduction

The high standard of living that many nations enjoy relies upon the existence of inexpensive fossil fuels to drive growth in their economies. The continued rise in the demand for fossil fuels will yield further increases in their price. This will slow economic growth and speed the extraction of unconventional oil. The increased fuel costs, coupled with the environmental harm resultant from conventional and unconventional fossil fuel use will reduce the standard of living for many people. A potential solution lies in the development of inexpensive renewable energy. A promising technology that is explored in this paper is micrometer scale rods composed of photovoltaic (PV) materials.

Microrods made of PV materials can be oriented vertically and arranged in arrays that are strongly absorbing of incident electromagnetic radiation[1]. These arrays can be used to generate electricity like a conventional PV cell. They can also be immersed in water to form part of a photoelectrochemical (PEC) device. The purpose of a PEC device is to generate hydrogen from solar energy by splitting water using PV-driven electrolysis. This hydrogen can be utilized as a fuel directly or reformed into hydrocarbon fuels.

This paper explores computational optimization using ray tracing as a means to enhance optical absorbance of microrod arrays. The rod's center-to-center spacing (pitch) and grid pattern types have been varied to maximize light absorbance from a variety of incident angles.

This paper also investigates how bubbles of oxygen evolving on the surface of the microrod arrays will scatter light before it reaches the microrod arrays. It quantifies how much light is reflected away from the rods as a function of incident angle, so that the reduction in energy available for harvest can be predicted.

These results are part of an ongoing effort by the author to characterize the interaction of light with the PEC device being developed by the Joint Center for Artificial Photosynthesis (JCAP). Future work will focus on further characterizing the interplay between light, gas bubbles and heat within the device. The aim of such efforts is to optimize device efficiency and longevity, as well as understand how other chemical and physical processes within the PEC device are affected by temperature changes.

2. Review of Photoelectrochemical Device Design and Chemistry

2.1 PEC Design

PEC devices of varying morphologies and chemical reaction pathways have been investigated since TiO_2 was used as a photoanode to split water in 1972[2]. Many of the geometries that have been investigated to date fall into several broad categories. The first involves the use of planar PV cells that are submerged in water and exposed to light.

---

[1] Michael Kelzenberg et al. "Enhanced absorption and carrier collection in Si wire arrays for photovoltaic applications," *Nature Materials* 9 (2010), 241.

[2] Ryu Abe. "Recent Progress on photocatalytic and photoelectrochemical water splitting under visible light irradiation," *Journal of Photochemistry and Photobiology C: Photochemistry Reviews* 11 (2010) 179.

Chemical reactions then proceed at catalyst sites, either on the surface of the PV cells or in a separate part of the PEC device (see Figure 1). Hydrogen and oxygen evolution occur in separated compartments of the device. Another category of PEC devices uses granules of PV material that are suspended in fluid or packed into a fluidized bed. The system is then illuminated and water is pumped through (see Figure 1) so that hydrogen gas may be collected. There is a potential for explosion and back-reactions because oxygen is evolved in the same location as hydrogen. Therefore, this is a less than optimal device. Yet another category involves using porous mat-like structures made of randomly oriented PV fibers. The mat is illuminated and water is pumped through it to achieve the same effect as the fluidized-bed type reactor[3]. Other designs exist in addition to these; this paper will focus on the rod-like structure depicted in Figure 2. This structure will be discussed later in more detail.

2.2 PEC Chemistry

A common reaction pathway used to split water into hydrogen and oxygen in a PEC device proceeds in three steps[4]. In the first step, 4 photons above the band gap energy of the PV material must be absorbed to create 4 electron holes (h^o) and 4 electrons (e^-),

$$4h\nu \rightarrow 4h^o + 4e^-. \tag{1}$$

In step 2, the electron holes are employed to oxidize the water at the photoanode as follows,

$$4h^o + 2H_2O \rightarrow O_{2\,(g)} + 4H^+. \tag{2}$$

In step 3, the electrons produced in step 1 reduce the 4 hydrogen ions produced in step 2 at the cathode as follows,

$$4e^- + 4H^+ \rightarrow 2H_{2\,(g)}. \tag{3}$$

Note that reaction (3) is able to proceed with the absorbance of only 2 photons, but the reaction at step (2) requires 4 photons to be absorbed.

As indicated earlier, hydrogen and oxygen gas must be generated in separate locations so that they do not form explosive mixtures. In order to transport the H^+ ions from step (2) to the hydrogen evolution site in step (3), PEC devices often use proton-exchange membranes (PEMs) (see Figure 2). The PEM allows for transmission of H^+ ions from the oxidization to the reduction compartments of the PEC device. However, generally speaking, larger atoms and molecules such as oxygen and hydrogen cannot pass through the membrane.

---

[3] C. Carver et al. "Modeling and development of photoelectrochemical reactor for H_2 production," *International Journal of Hydrogen Energy* 30 (2011) 5-7.

[4] T. Bak et al. "Photo-electrochemical hydrogen generation from water using solar energy. Materials-related aspects," *International Journal of Hydrogen Energy* 27 (2002) 997.

At minimum, 1.23 eV of potential energy between electrons and electron holes is required to perform this reaction in pH 7 water at 300 K[5]. This energy corresponds to a photon wavelength of approximately 1,000 nm, in the infrared region of light. For reference, visible light falls between 380 - 780 nm, or approximately 1.6 - 3.3 eV. However, there are multiple losses of potential in a PEC device that increase the total required energy of the electron-hole pairs produced by the PV material to above 1.23 eV. This is caused by ohmic resistance losses within the PV and other electrically conductive

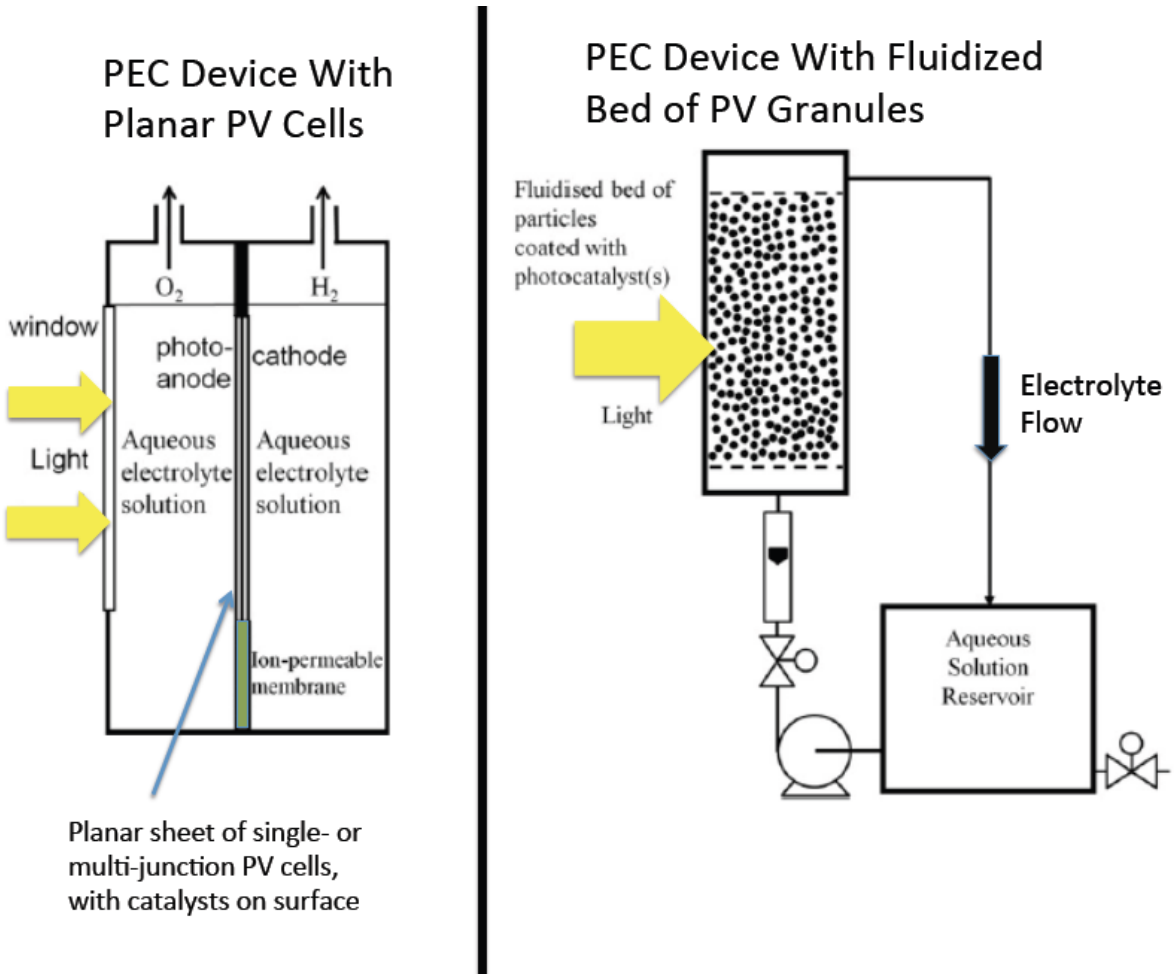

Figure 1: Photoelectrochemical devices containing planar photovoltaic cells (on left) and a fluidized bed of photovoltaic granules (on right)[6].

materials, resistance at various liquid-solid interfaces and ion charge transport losses in the electrolyte/membranes. Due to these compounded effects, the PV material in the PEC must produce a total of about 2 eV[7], in the absence of an external applied voltage bias.

---

[5] Carver, 1.
[6] Figures adapted from Carver, 5 and 7.
[7] Bak, 1000.

2.3 Constraints on Photovoltaic Materials in a PEC

The voltage required for electrolysis in a PEC device creates fundamental constraints on the type of PV material that can be used. Silicon cells, for example, have a band gap of 1.1 eV for crystalline and 1.7 eV for amorphous crystal structures, which is below the 2 eV needed for spontaneous water splitting. Additionally, PV materials exposed to the electrolyte must be corrosion resistant. This is due to the corrosive nature of the electrolyte, electrons, holes and H^+ ions generated in the PEC device[8]. Therefore, many conventional single junction semiconductors are of no use in PEC systems. At the time of writing, colleagues of the author were trying to develop multi-junction PV cells for use in PEC devices. However, this paper will focus only on single junction systems.

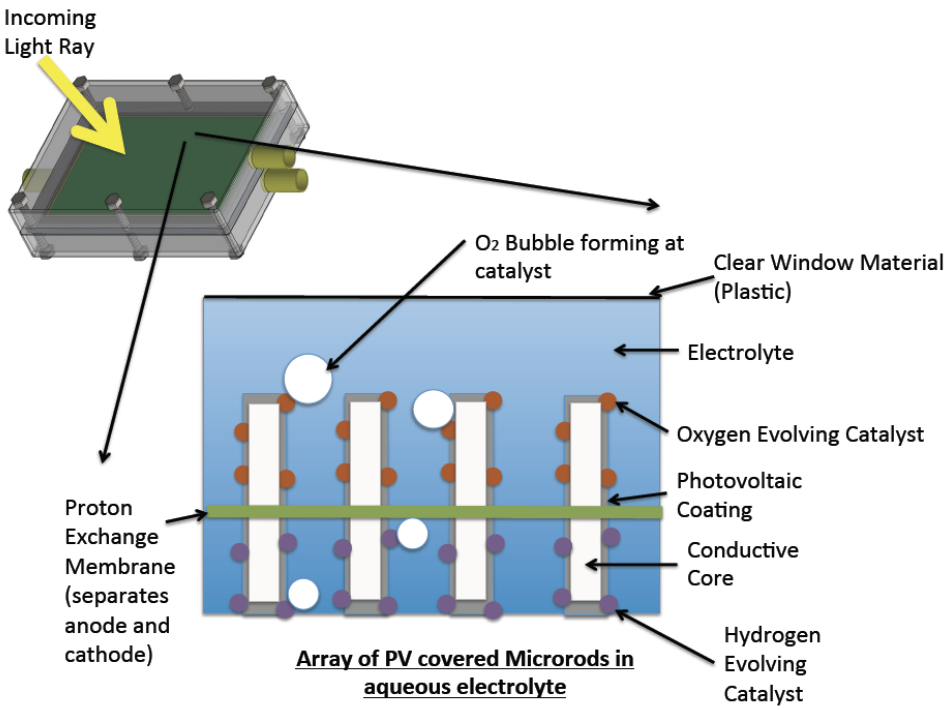

Figure 2: Microrod array containing photoelectrochemical device. A view of the device as a whole is provided on the upper left, while an enlarged view of a section of the microrod array and proton exchange membrane is provided on the bottom right.

Problematically, any single junction PV material that has a high band gap exhibits lower efficiency than the lower band gap materials used in most PV cells. This loss in efficiency arises because the solar insolation available on the earth's surface has a spectrally varying intensity. This issue is illustrated in Figure 3. If one selects a material that has a high band gap, then the majority of the light that falls upon the earth will fail to produce photocurrent in the PV cell. Conversely, lower band gap materials have greater current output, but lower voltage output. There exists a trade off between a PV cell's voltage and current output, which must be optimized to attain maximum efficiency.

[8] Bak, 995.

The optimal band gap for a single-junction solar cell under illumination by the electromagnetic spectrum present at the top of earth's atmosphere is approximately 1.3 eV[9]. Following from Ohm's law, a PV cell's efficiency can be characterized as

$$\eta = \frac{J_m V_m}{P_s}, \qquad (4)^{10}$$

where J_m and V_m are the current at the cell's maximum power point and P_s is the power of the radiation incident on the cell.

Of the known semiconductors that have been studied for use in PEC devices, oxides such as TiO_2, WO_3 and $BiVO_4$ are commonly investigated in literature. This is due to their favorable corrosion resistances and band gap energies[11]. Strontium Titanate ($SrTiO_3$) is a material that has also drawn the attention of researchers, and it was the material that comprised the rods simulated by the author. Single crystal, undoped samples of $SrTiO_3$ have a band gap of approximately 3.22 eV[12], which is almost within the UV spectrum. As such, a PV cell using $SrTiO_3$ is inefficient (see Figure 3). Therefore, if $SrTiO_3$ is used in a PEC device, very high levels of optical absorbance must be ensured to maximize hydrogen gas output.

3. Microrod Array Structure and Advantages

3.1 Microrod Geometry Overview

Figure 4 provides a depiction of the microrods that were simulated in the modeled system. Each rod was nominally 100 μm tall and had a diameter of 10 μm. The rods contained a nickel core that would serve as a charge collection site for electrons and also provide a junction with the $SrTiO_3$ to facilitate charge separation. The rod was coated in a thin (~850 nm) layer of $SrTiO_3$, the active PV layer.

3.2 Catalyst Considerations

The use of microrods in a PEC device provides sufficient surface area for both light absorbance and hydrogen gas evolution. The chemical reactions that take place in the modeled type of PEC device occur on the rod surfaces, at the catalyst sites (see Figure 2 for a depiction of these catalysts). If the catalyst sites have insufficient aggregate surface area, the rate of water splitting chemical reactions will be too slow. This will increase the rate of electron-hole pair recombination (see more discussion on recombination below), which will result in lower device efficiency[13]. On the other hand, these catalysts sites will reflect and absorb some of the light that is incident on the rods, preventing it from

---

[9] Gerardo Araujo and Antonio Martí. "Absolute limiting efficiencies for photovoltaic energy conversion," *Solar Energy Materials and Solar Cells* 33 (1994) 213.
[10] Jenny Nelson. The Physics of Solar Cells. London: Imperial Press, 2003. 12.
[11] Abe, Carver, Bak.
[12] Manuel Cardona. "Optical Properties and Band Structure of SrTiO3 and BaTiO3," *Physical Review* 140 (1965) A651.
[13] Carver, 3.

reaching the PV material. The use of rods enhances the total percentage of the PV material in the system that is exposed to incident light relative to conventional, planar PV cells. This allows for the proper catalyst loading, coupled with good light absorbance. As will be discussed later, these surface catalysts can also facilitate light scattering within the system, which can aid the light absorbance process.

3.3 Decoupling of Light Absorbance and Charge Transport

Even without considering surface catalysts, the use of microrod arrays offers several advantages for enhancing energy harvesting over other PV cell morphologies. In any PV device, light must travel a sufficiently long path through the active material for it to be absorbed, per the Beer-Lambert law,

$$I_{Transmitted}(x) = Io * \exp\left(-\frac{4\pi k(\lambda)x}{\lambda}\right), \tag{5}$$

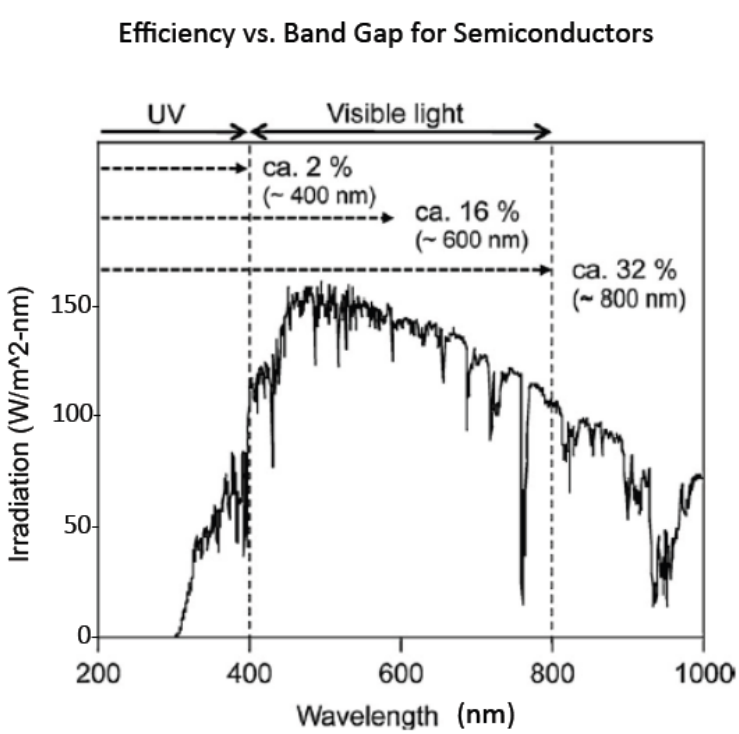

Figure 3: PEC device maximum efficiency vs. band gap, if 100% quantum efficiency is assumed[14]. Note that incorporating $SrTiO_3$ (band gap ~380 nm) into any PEC device results in a low maximum theoretically attainable efficiency. Spectrum presented is AM 1.5.

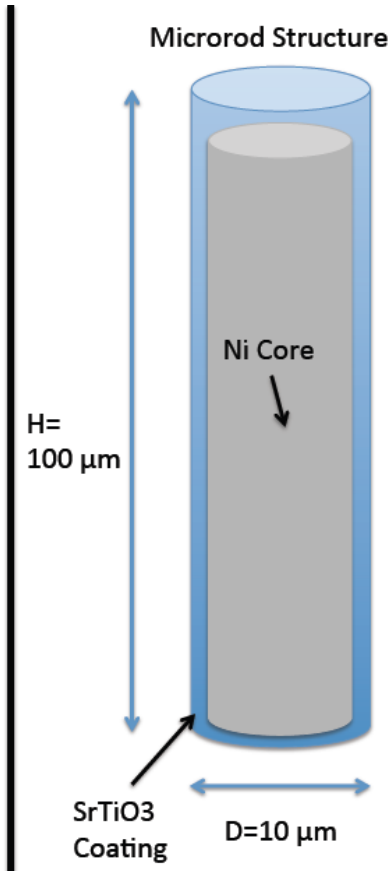

Figure 4: Depiction of microrod structure. Figure not drawn to scale.

[14] Abe, 180.

where Io is the initial intensity of light incident upon a surface (W/m^2), $I_{Transmitted}(x)$ is the intensity after transmission through a path of length x, λ is the wavelength of the incident light and k(λ) is the wavelength-dependent imaginary part of a material's refractive index known as the attenuation coefficient (see equation (18)). This equation is valid when k is not a function of the spatial location within a material. The longer path light takes through a PV material, the more it can be absorbed and converted into electrical power. For most semiconductors, nearly perfect absorbance occurs with a material thickness of a few tens or hundreds of microns[15].

When a PV material absorbs a photon, the resulting electron and hole can only travel a certain average distance before they undergo a recombination process. After recombination, the electron or hole returns to its original energy state, prior to excitation by a photon. The recombined hole or electron can no longer be used to drive an external circuit, and thus is of no use. This average distance before recombination is known as the minority-carrier diffusion length. There are several processes that can cause recombination, but a general equation that gives the diffusion length is

$$L_{Diffusion} = \sqrt{D_{E,H} * \tau_{E,H}}, \qquad (6)^{16}$$

where $D_{E,H}$ is the diffusion coefficient of the electron or hole in the semiconductor material and $\tau_{E,H}$ is the lifetime of the electron or hole, respectively. The electron or hole travels at some finite average velocity through the semiconductor's crystal lattice. The shorter distance it travels before being collected by an external circuit, the more likely that its travel time will not exceed $\tau_{E,H}$. Therefore, one would like a photovoltaic material to be as thin as possible so as to lose the fewest electron-hole pairs to recombination.

Employing a rod-like microstructure allows for both good light absorbance and good charge collection by decoupling the absorbance and charge collection processes[17]. A photon that enters a rod from a trajectory that is close to normal to the plane of the microrod array travels a long path through the photovoltaic material. This enhances the photon's chance of absorbance. Once the photon is absorbed, the resulting electron and hole only need to travel a short distance, orthogonal to the direction of the major axis of the rod, before they can be used. This process is illustrated in Figure 5. Theoretically, for homogeneous rod structures, the optimal rod diameter is on the order of the minority-carrier diffusion length[18].

3.4 Light Trapping in Microrods

Light trapping is another phenomenon that is used advantageously by microrods. When a rod is made of a material possessing a higher index of refraction than the surrounding

---

[15] Nelson, 36.
[16] Nelson, 115.
[17] Emily Kosten, Emily Warren and Harry Atwater. "Ray optical light trapping in silicon microwires: exceeding the $2n^2$ intensity limit," *Optics Express* 19 (2011) 3317.
[18] L. Tsakalakos et al. "Silicon nanowire solar cells," *Applied Physics Letters*, 91 (2007) 3.

medium from which light is incident, the light that has already entered a rod can undergo total internal reflection such that it will never escape the rod surface back into the surrounding medium. The definition of the index of refraction of a material is

$$n_{\text{Medium}} = \frac{C}{V_{\text{Light in Medium}}} = \sqrt{\frac{\epsilon\mu}{\epsilon_f\mu_f}}, \tag{7}$$

where C is the speed of light in a vacuum ($2.9979*10^8$ m/s), ϵ is the electric permittivity in the medium, ϵ_f is the free space electric permittivity ($8.8542*10^{-12}$ C/N-m), μ is the magnetic permeability of the medium and μ_f is the free space magnetic permeability ($4\pi*10^{-7}$ Wb/A-m). Total internal reflection will occur if the ray within a rod strikes the rod's surface at an angle, measured from the rod's surface normal, which is greater than the critical angle (see Figure 5). The critical angle is defined as

$$\theta_c = \sin^{-1}\left(\frac{n_o}{n_{rod}}\right), \tag{8}$$

where n_o is the index of refraction of the medium around the rod and n_{rod} is the index of refraction in the PV layer of the rods. Equation (8) is derived from Snell's law, which is presented later as equation (17). This phenomenon allows for the optical path of light within a rod to be greatly enhanced, which increases absorbance, per equation (5). It should be noted that most PV cells exploit this same effect through various means.

3.5 Intra-rod Light Scattering

The previously described ways in which microrod structures enhance absorbance apply to individual rods. Especially when the area fraction occupied by rods in an array viewed from an areal perspective (AF) is low, however, much of the incident radiation on an array does not immediately encounter a rod after entering the array's spatial domain. Careful choice of the pitch and grid pattern type increases the chance that an incident light ray will encounter a microrod and reflect multiple times from one rod to another before exiting the array's domain (see Figure 6).

Every time a ray is reflected, a portion of its intensity is reflected and a portion is absorbed by the rod. Sometimes, a portion of the ray's intensity is transmitted through the rod. This is shown below[19],

$$I_{\text{Absorbed, Ray}} = Io * \sum_{Nref}\left(1 - R_i(\theta_o, \theta_t, n_o, n_t)\right) * (1 - I_{\text{Transmitted},i}(x)). \tag{9}$$

The ray's initial energy is denoted Io. The percent of the ray's energy that is reflected each time is denoted $R_i(\theta_o, \theta_t, n_o, n_t)$, where $0 \le R_i(\theta_o, \theta_t, n_o, n_t) \le 1$. The portion that is transmitted through the rod is $I_{\text{Transmitted},i}(x)$, where $0 \le I_{\text{Transmitted},i}(x) \le 1$. $1-I_{\text{Transmitted}}(x)$ gives the portion that is absorbed in the PV material (see equation (5)). The sum of intensity of the transmitted, reflected and absorbed rays equals the intensity of the incident ray. As N_{ref}, the number of reflections that the ray undergoes, increases,

[19] Equation adapted from Nelson, page 254.

more of the incident ray energy is absorbed. One therefore wishes to maximize the number of reflections that a ray undergoes after it enters the microrod array.

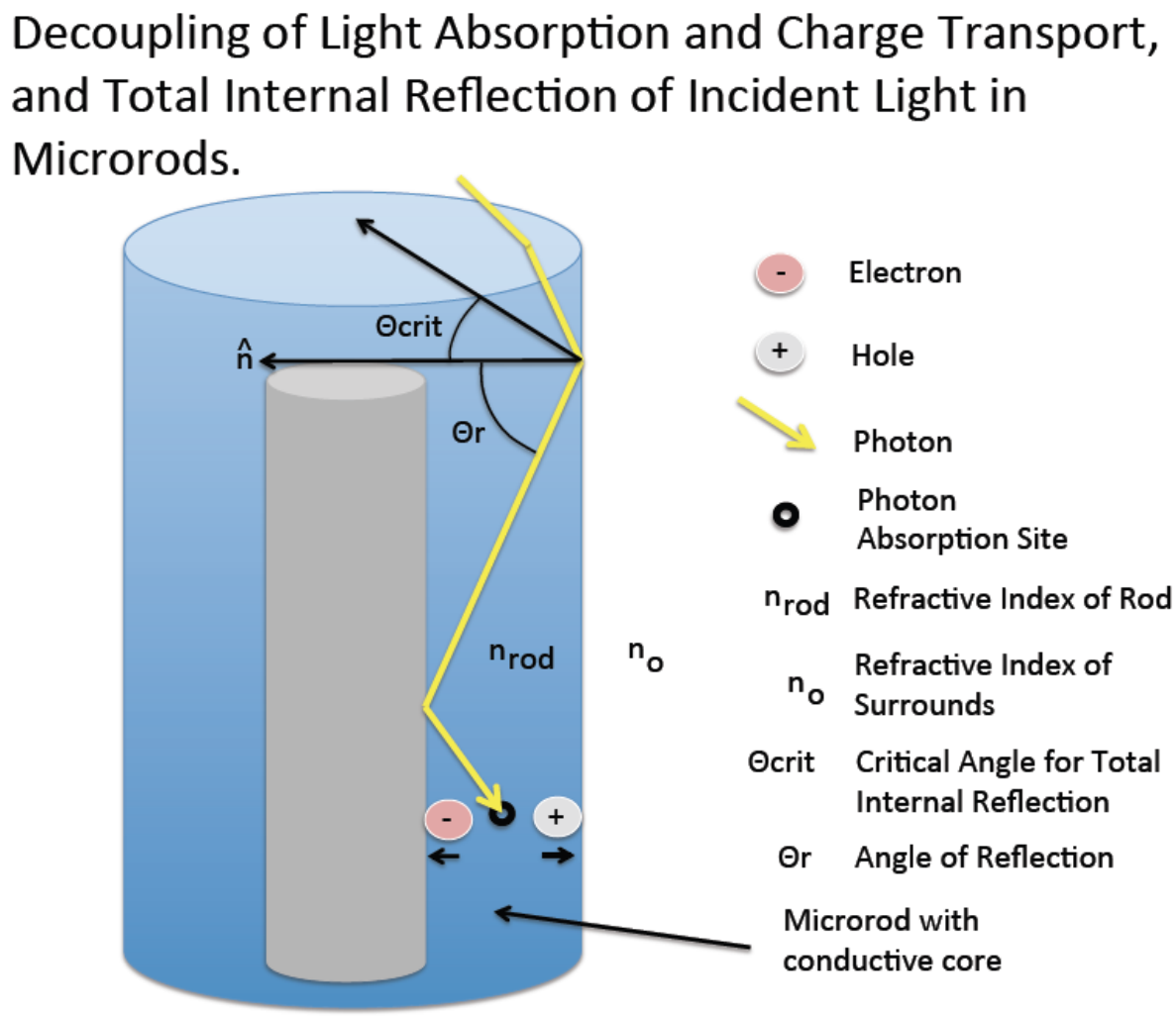

Figure 5: Depiction of advantageous optical and electrical properties of PV microrods. If light is transmitted into rod, it will repeatedly reflect internally if the angle of reflection is greater than the critical angle. Once the light is absorbed, the charge collection process is not as prone to recombination as in planar PV cells, due to the orthogonal pathways of light and electron-hole pairs.

3.6 Material Conservation Considerations

A final benefit of using microrod arrays is the lower volume of PV material needed to achieve optical absorbance approaching that of conventional, planar PV cells[20]. Especially when exotic PV materials must be used in a PEC device, this can become a crucial, cost reducing advantage.

[20] Kelzenberg, 241.

4. Theories in Optics Modeling

Two classes of optics that pertain to microrod arrays are physical optics and geometrical optics (ray tracing). The difference between these approaches lies in their mathematical treatment of light, and the length scales at which their use is valid.

4.1 Physical Optics

Physical optics treats light as a wave, and is applicable for reflecting media of most size regimes. It is a valid approach for modeling microrods interacting with infrared, visible and UV light. Although physical optics can be used to model very large systems, its application becomes less attractive when ray tracing is a valid approach.

Physical optics solves for the amount of energy absorbed by a reflecting surface using Maxwell's equations, which can be written as

$$\nabla \times \mathrm{E} = -\frac{\partial \mathrm{B}}{\partial \mathrm{t}}$$

$$\nabla \times \mathrm{H} = \frac{\partial \mathrm{D}}{\partial \mathrm{t}}$$

$$\nabla \cdot \mathrm{D} = \rho$$

$$\nabla \cdot \mathrm{B} = 0. \tag{10}$$

In this system of equations, E is the electric field, H is the magnetic field, B is the magnetic field flux, D is the electric field flux and ρ is the charge density. Two other useful relations that relate these equations to the magnetic permeability and electric permittivity are

$$\mathrm{B} = \mu \cdot \mathrm{H}, \text{ and}$$
$$\mathrm{D} = \epsilon \cdot \mathrm{E}. \tag{11}$$

A full discussion of how to solve these equations is not given here. The solution of these equations for the boundary conditions present at the surfaces of the two media involved in a reflection yields E and H for the incident, reflected and transmitted light waves. These values then allow one to calculate S, the Poynting vector. S is defined as the energy flux traveling in an electromagnetic wave, through a surface perpendicular to the direction of travel, and is calculated as

$$\mathrm{S} = \mathrm{E} \times \mathrm{H}. \tag{12}$$

S is a rapidly varying function of time, but its norm is the energy within a ray of light. The direction of travel of the light wave is given as S divided by the norm of S,

$$\text{Direction of Ray Propagation} = \frac{\mathrm{E} \times \mathrm{H}}{\|\mathrm{E} \times \mathrm{H}\|} \tag{13}$$

Solving for the norm of S in the incident ray, reflected ray and the transmitted ray will indicate how much energy is absorbed by the microrods, and will also indicate the direction the ray travels through a system.

The primary advantage of solving Maxwell's equations is that the solutions they provide are highly accurate, even in complex, microscale and nanoscale systems. The disadvantage is that the solution of these equations is not trivial, and becomes computationally demanding for any large-scale, high frequency system.

4.2 Geometric Optics

Geometric optics, or ray tracing, treats light as a particle. This approach is generally considered valid when $\lambda \leq 10 * d$, where d is the smallest dimension of a reflecting body. At first glance, this approach would seem perfectly valid for rods made of $SrTiO_3$ having diameters of 10 μm, as the wavelengths of interest would lie below the band gap, i.e. $\lambda \leq 0.38$ μm.

Ray tracing uses a number of equations to predict the trajectory of and net energy loss from rays of light as they propagate through a system. Upon encountering any infinitely smooth reflecting surface, a ray that makes an angle θ_o with the surface's normal will reflect such that

$$\theta_r = \theta_o, \tag{14}$$

where θ_r is the angle that the reflected ray makes with the surface normal. If the vector of the incident ray's velocity is known, then the reflected velocity vector is given by

$$V' = V - 2 * (v \cdot \hat{n}) * \hat{n}, \tag{15}$$

where V' is the reflected vector, V is the incident vector and $\hat{n}$ is the surface normal. The normal of any surface that can be represented mathematically as $f_{Surf}(x, y, z)$ is, in Cartesian coordinates,

$$\hat{n} = \frac{\nabla * f_{Surf}(x,y,z)}{||\nabla * f_{Surf}(x,y,z)||}. \tag{16}$$

When a ray reflects, usually some of the ray's energy will transmit into the reflecting surface. The angle that this transmitted ray makes with the surface normal, θ_t, is calculated using Snell's law,

$$n_t * \sin(\theta_t) = n_o * \sin(\theta_o), \text{ which can be rearranged as}$$

$$\theta_t = \sin^{-1}(n_o * \sin(\theta_o) / n_t), \tag{17}$$

where n_t is the refractive index of the reflecting surface and n_o is the refractive index of the medium from which the ray is incident. The relationship between $\hat{n}$, θ_o, θ_r, and θ_t is illustrated in Figure 7.

The definition of the refractive index of a material was given in equation (7). Broadly speaking, there are two classes of materials in optics: dielectrics, which are perfect electrical insulators that are transparent to light, and absorbing media, which absorb light that transmits through them (this absorbance is of the Beer-Lambert type, given in equation (5)). Dielectric media have an index of refraction that is entirely real, while the index of refraction of an absorbing medium has an imaginary component,

$$n_{\text{Absorbing Medium}}(\lambda) = (n_{\text{Real, medium}} - j * k_{\text{medium}}), \tag{18}$$

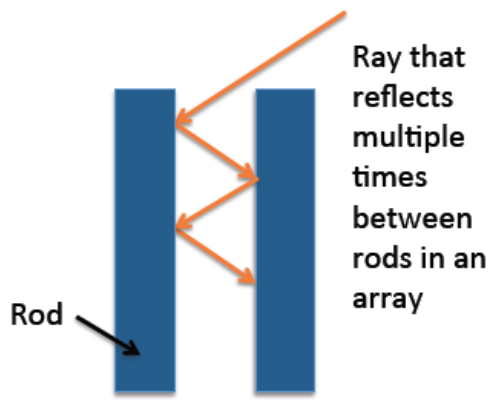

Figure 6: Multiple ray reflections in microrod array

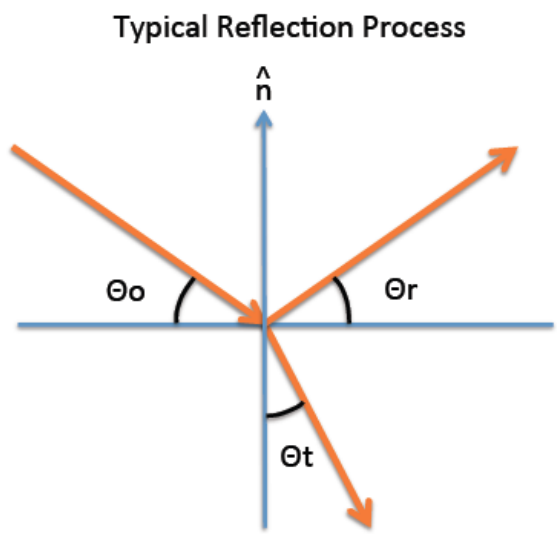

Figure 7: Depiction of ray reflection for smooth surfaces

where j=√-1. Most substances exhibit dielectric behavior for some wavelengths of electromagnetic radiation and absorbing behavior for others, hence the index of refraction of most substances is a function of wavelength, as well as other variables.

The use of equation (17) becomes invalid when any of the media involved are absorbing, because θ_t becomes a non-physical quantity with imaginary terms. This presents obvious problems if one is analyzing transmission of light through PV material that, by design, is absorbing of incident light. An assumption to deal with this issue is detailed later.

In order to calculate the reflectivity of a surface for unpolarized incident light, R, one can use the Fresnel relations as follows,

$$R = \frac{1}{2}(r_{\text{perp}}^2 + r_{\text{parr}}^2), \text{ where}$$

$$r_{\text{perp}} = \frac{\frac{n_o}{\mu_o} * \cos(\theta_o) - \frac{n_t}{\mu_t} * \cos(\theta_t)}{\frac{n_o}{\mu_o} * \cos(\theta_o) + \frac{n_t}{\mu_t} * \cos(\theta_t)}, \text{ and}$$

$$r_{parr} = \frac{\frac{n_t}{\mu_t}*\cos(\theta_o) - \frac{n_o}{\mu_o}*\cos(\theta_t)}{\frac{n_o}{\mu_o}*\cos(\theta_o) + \frac{n_t}{\mu_t}*\cos(\theta_t)}. \quad (19)$$

For most materials, the magnetic permeability is equal to the free space magnetic permeability, i.e. $\mu_o = \mu_t = \mu_f$.

The biggest advantage of using ray tracing is that it is computationally simple relative to physical optics, as the Maxwell equations that govern the propagation of electromagnetic radiation are not needed. As such, ray tracing can be used to model very large systems in a computationally inexpensive manner. The disadvantage is that its use requires one to make a number of assumptions about and/or restrictions on the attenuation coefficient ($k(\lambda)$), dimensions and surface roughness of media in a modeled system.

5. Computational Scheme for Modeling Light Absorbance in Microrod Arrays

The author created a time-marching, explicit, ray tracing computational scheme to model the microrod arrays, which is presented below. Aspects of this scheme other than the treatment of material properties, the calculation of thin film reflections, rod grid generation and the convergence scheme used to pinpoint a ray's reflection location were based on work by Zohdi[21].

5.1 Ambient Environment

In addition to the rod geometry, dimensions and material composition detailed above, the surrounding media around the rods was modeled to be pure, pH 7.0 water at 300 K. The water was assumed to be dielectric, which is reasonable given the extremely low attenuation of coefficient of water at 385 nm, the modeled incident light's wavelength.

5.2 Thin Films

The primary hurdle for using ray tracing for the author's simulations of light absorbance by microrods was that some of the dimensions encountered in the array are below those applicable for ray tracing. Specifically, in the modeled rods, the layer of $SrTiO_3$ was 850 nm thick. This was problematic for multiple reasons.

The treatment of light as a particle that is fundamental to ray tracing becomes invalid when the dimensions of the reflecting surfaces become too small. Typically, when light encounters a thin film whose thickness on the order of its wavelength, it behaves like a wave as it is reflected off of the film's interfaces with adjacent materials. A single ray entering a series of thin film layers will emerge as multiple rays, with a new ray generated at each material interface (see Figure 8). The number of rays in a simulation

[21] T. I. Zohdi. "Modeling and simulation of the optical response rod-functionalized reflective surfaces," *Computational Mechanics*, 50 (2012) 257-268.

increases, and interference between reflected wavefronts becomes an issue[22]. This invalidates the Fresnel relations for calculating reflectivity that were presented earlier.

A method had to be employed to reduce the computational complexity that arose from the growth of the number of rays at each reflection, and to characterize the reflectivity of thin films. The author chose to use the matrix method for calculating reflectivity. This is a title that applies to a class of computation in optics. This method can be employed to give an overall reflectivity for a series of thin film layers, and can allow one to treat the reflection as if only one ray emerges from the layers. A specific application of this method that is detailed by Heavens[23] is given below (see Figure 8 for description of terms involving n, k and d),

$$g_1 = \frac{n_o^2 - n_1^2 - k_1^2}{(n_o + n_1)^2 + k_1^2}$$

$$h_1 = \frac{2n_o k_1}{(n_o + n_1)^2 + k_1^2}$$

$$g_2 = \frac{n_1^2 - n_2^2 + k_1^2 - k_2^2}{(n_2 + n_1)^2 + (k_2 + k_1)^2}$$

$$h_2 = \frac{2(n_1 k_2 - n_2 k_1)}{(n_2 + n_1)^2 + (k_2 + k_1)^2}$$

$$\alpha_1 = \frac{2\pi k_1 d_1}{\lambda}$$
$$\gamma_1 = \frac{2\pi n_1 d_1}{\lambda}$$

$$p_2 = e^{\alpha_1} \cos(\gamma_1)$$
$$q_2 = e^{\alpha_1} \sin(\gamma_1)$$

$$t_2 = e^{-\alpha_1}(g_2 \cos(\gamma_1) + h_2 \sin(\gamma_1)$$
$$u_2 = e^{-\alpha_1}(h_2 \cos(\gamma_1) + g_2 \sin(\gamma_1)$$

$$p_{12} = p_2 + g_1 t_2 - h_1 u_2$$
$$q_{12} = q_2 + h_1 t_2 - g_1 u_2$$
$$t_{12} = t_2 + g_1 p_2 - h_1 q_2$$
$$u_{12} = u_2 + h_1 p_2 - g_1 q_2$$

[22] O.S. Heavens. Optical Properties of Thin Solid Films. New York: Dover Publications, 1991. 56.
[23] Heavens, 74-79.

$$R = \frac{t_{12}^2 + u_{12}^2}{p_{12}^2 + q_{12}^2}. \quad (20)$$

In these equations, γ_1 has units of radians.

It should be noted that these equations only apply for reflectivity from normal incidence, but they were used for all reflections in the system. Many other relations exist for reflections from thin films, but they either assume that the layers are dielectric, or that their attenuation coefficient is so high (e.g. for metals) that certain terms can be ignored, allowing for the effect of angle of incidence to be quantified[24]. It was problematic to assume normal incidence in the model because reflectivity from any surface tends to increase as the angle at which light strikes a surface increases (measured with respect to a surface's normal). This reliance on mathematically simple methods for predicting system behavior represents a deficiency in the author's model that is addressed in the Future Modeling and Experimental Work section of this paper.

Another problem presented by the presence of thin films in the modeled system was that the material properties for a thin film of any substance tend to differ from that of bulk samples. Additionally, the optical properties of a thin film are highly dependent upon its specific deposition method, annealing process and substrate[25]. To the knowledge of the author, there have been no studies that measure or predict the optical properties of thin $SrTiO_3$ films deposited on Ni. Additionally, at the time or writing, $SrTiO_3$ was generally poorly characterized in scientific literature from an optical standpoint compared to, for example, Si. This is likely due to $SrTiO_3$'s inherent lack of efficiency as a PV material relative to other, more earth-abundant materials. It has been found that the real and imaginary components of the index of refraction of $SrTiO_3$ thin films within the visible light spectrum were lower than those of bulk samples for several film deposition techniques[26]. The author's colleagues did not yet know the exact deposition methods that would be used to create the $SrTiO_3$ layer on the microrods at the time of writing. This led to using the material properties of undoped, single crystal samples of $SrTiO_3$ at 300 K as an estimate.

Generally, $SrTiO_3$ is unlikely to be incorporated into a final design owing to its inherent inefficiency. Hence, some of the above issues may eventually become moot and new models must be constructed to more accurately capture the system behavior.

5.3 Modeling Ray Energy Absorbance from Reflections

The initial intensity, Io, of each of the rays used in the simulation was set equal to an arbitrary quantity. The arbitrary nature of Io was not important, as the total average percentage of Io that was absorbed across all rays was the figure of merit output by the simulation. Each time a ray underwent a reflection, the loss in intensity was calculated

---

[24] Heavens, 53-73.

[25] B.G. Almeida et al. "Determination of infrared optical parameters of $SrTiO_3$ thin films from the reflectivity spectrum," *Thin Solid Films* 513 (2006), 275.

[26] Hübert, Thomas, Uwe Beck, Helga Kleike. "Amorphous and nanocrystalline $SrTiO_3$ thin films," *Journal of Non-Crystalline Solids* 196 (1996), 153.

using equation (9). The reflectivity used in this equation was calculated with the matrix method given above (equations (20)).

To aid computational simplicity, it was assumed that all of the ray energy transmitted into a rod upon reflection became absorbed within the rod. This was done because calculation of the transmission angle, θ_t, is not possible for absorbing media using Snell's law (equation 17)). Given the chance for total internal reflection within the rods, this seemed like reasonable assumption.

5.4 Simulation of Microrod Geometry

The microrods simulated in the model were generated using prolate ellipsoids. The surface equation of a prolate ellipsoid is

$$\left(\frac{x-xc}{a}\right)^2 + \left(\frac{y-yc}{b}\right)^2 + \left(\frac{z-zc}{c}\right)^p = 1 = f(x, y, z, a, b, c, p), \quad (21)$$

where x, y, and z are the set of spatial coordinates that define the surface of the ellipsoid; xc, yc and zc define the centroid of the ellipsoid; a, b and c define the major and minor radii of the ellipsoid (for prolate geometry, a=b<c) and p is set such that p >> 2. In the simulation, p=70. Setting p to this high value caused the ellipsoid surface to resemble a cylinder. Figure 9 gives an example of an ellipsoid generated with this equation.

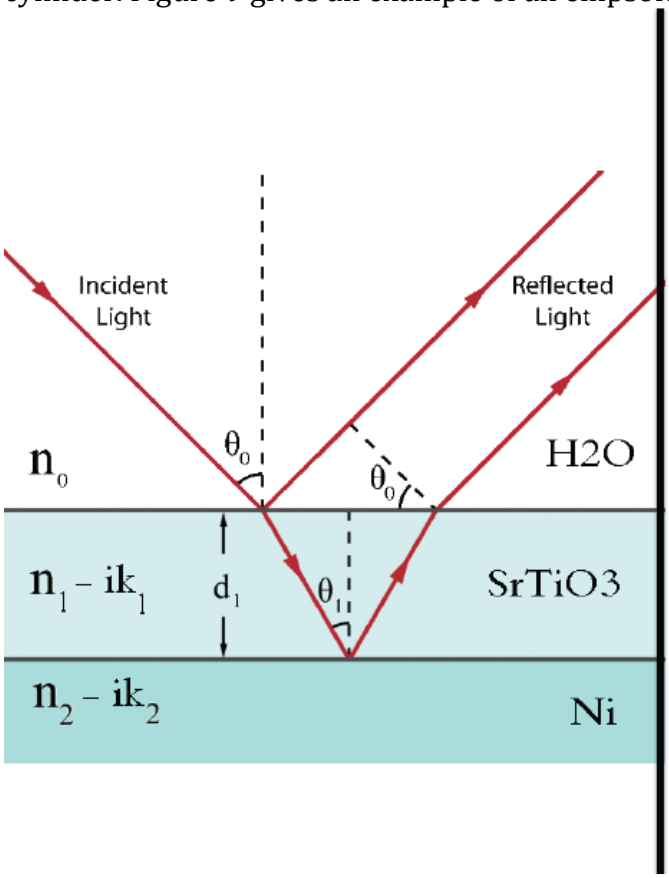

Figure 8: Multiple ray emission from reflection processes in thin film media.

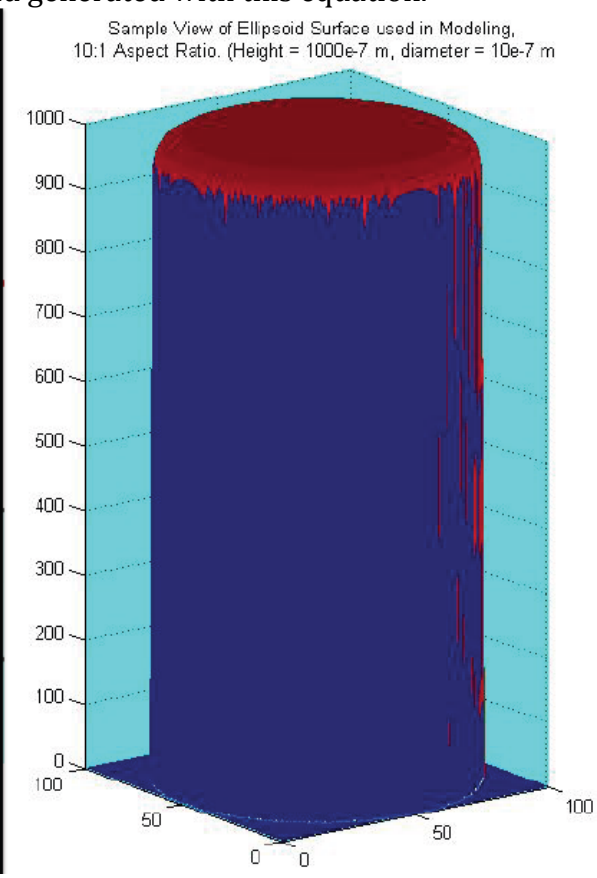

Figure 9: Depiction of ellipsoid like those used in the simulation

Equation (21) can be plugged into equation (16) to determine an ellipsoid's surface normal at a specific location, which was needed to compute the trajectory of a reflected ray. Ellipsoids provide a useful computational tool for simulating a variety of different shapes, though cylinders were the only geometries modeled in this simulation.

5.5 Microrod Array Grid Generation

In order to simulate a microrod array, a grid of ellipsoid centroids (xc_n, yc_n, zc_n) was generated, where the subscript n denotes rod number. The specific grid type was dictated by the pattern and pitch desired before each run. The two classes of grid pattern simulated in this model were (equilateral) triangular and square grids, images of which are shown in Figure 11. Pitch was varied from 14 to 20 μm in 1 μm increments. Smaller pitches were not investigated so that the gap between two adjacent rods would not be less than 4 μm. Otherwise, the criteria for using ray tracing (that $\lambda < 10*d$) would be violated for the 385 nm wavelength light simulated in the model. Modeling of larger pitches was attempted, but the results are not presented due to these designs' poor light absorbance. The total number of rods in an array varied from simulation to simulation, because the number of rods in the array was given by

$$N_{\text{Rows, Square Array}} = \text{round}(L/\text{pitch})$$

$$N_{\text{Columns, Square Array}} = \text{round}(L/\text{pitch})$$

$$N_{\text{Rows, Triangular Array}} = \text{round}(L/(\frac{\text{pitch}}{2}))$$

$$N_{\text{Columns, Triangular Array}} = \text{round}(L/(\frac{\text{pitch}}{\sqrt{3}/2}))$$

$$N_{\text{Rods}} = N_{\text{Rows}} * N_{\text{Columns}}, \tag{22}$$

where L, the length of the array on one side, is 10 cm. Thus, as pitch decreased, the number of rods increased. The number of rods in a square grid of pitch =20 μm, for example, was 5000*5000, or $25*10^6$ total rods. The author chose to model the entire microrod array grid rather than a smaller selection of rods. This was done because a light that enters an array at an oblique angle (closer to Φ=90°; see section 5.7 below for more detail) can encounter rods that are quite far from the light's initial point of entry, unless the light enters close to the array's edge. Given the large number of rods in the actual array that would be built, however (see below), the number of rays that would enter near the array edges would be small compared to the total number that would enter the array.

5.6 Setting and Tracking Ray Position as a Function of Time

In order to increment ray position at each time step, the following explicit scheme was used.

$$x_{i+1} = x_i + V_{\text{Light in Medium, x}} * \Delta t$$

$$y_{i+1} = y_i + V_{\text{Light in Medium, y}} * \Delta t$$

$$z_{i+1} = z_i + V_{\text{Light in Medium, z}} * \Delta t, \tag{23}$$

where the subscript i denotes the time step, x, y and z denote ray position and Δt is the time step. The time step size was given by the following formula,

$$\Delta t = \xi * \frac{L_{Max}}{|V_{\text{Light in Medium}}|}, \tag{24}$$

where $0.05 \leq \xi \leq 0.1$ and L_{Max} was the largest dimension of the simulated microrod array. ξ was chosen to be 0.05, and L_{Max} was 10 cm, as this is the length of the square microrod array that will eventually be built by the author's colleagues.

The initial z locations of the rays were set to be 1.01*h, where h was the rod height (100 μm). The initial x and y domain of the rays was a circular region of diameter equal to 10*pitch. The rays' individual x and y coordinates were randomly placed within this circular domain. The centroid of this domain was chosen to be at the center of the array, i.e. at (5 cm, 5 cm).

The number of rays, N, that were incident upon the array was determined by continually increasing N until the average calculated absorbance only changed within a small tolerance. For all simulations, N rays=3,000.

5.7 Setting Initial Ray Propagation Direction

The position of the sun changes with the time of day, time of year and the latitude from which one observes the sun's passage. The position of the sun is typically given in terms of two angles, θ and Φ, as depicted in Figure 10 below. θ is known as the solar azimuth, and is measured with respect to solar north. For example, when θ=180°, the sun is shining from the south, when θ=90°, the sun is shining from the east, and so on. Φ, the solar zenith angle, is measured from the zenith, such that when Φ=0°, the sun is directly overhead the observer, and when Φ=90°, the sun is on the horizon.

In order to simulate a wide range of possible incident angles, the range of Φ was varied from 0° to 82.5°, in 7.5° increments. It should be noted that the actual solar azimuth angles at which light will enter a PEC device would be dependent upon the window material and electrolyte present in the PEC device. Using Snell's law (equation (17)), one can show that the apparent solar zenith angle of any incident ray will be reduced in the device relative to its trajectory in the atmosphere. In other words, the rays will bend towards being incident at Φ=0°. However, owing to the scattering effect of bubbles in the device, some of the incident light will be scattered towards Φ=90° after entering the device. Hence, this wide range of investigated trajectories for the microrod array is valuable.

In square and triangular grid arrays, the absorbance was periodic because of the periodic nature of the grid arrays. In square arrays, the full variation in absorbance was

observed in a 45° range of θ. This is illustrated in Figure 11 below. For the square array, θ was varied from 135° to 180°, in 5° increments. For triangular arrays, the full range of absorbance was observed in a 60° range of θ. For a triangular array, θ is varied from 120° to 180°, in 5° increments. This range of θ and Φ was evaluated for each simulation, providing the plots presented in the results section.

5.8 Modeling Reflection Locations From Ellipsoids

In order to determine if a ray in the microrod array contacted a rod, the author plugged the (x,y,z) spatial coordinates of the ray into the equation for an ellipsoid (equation (21)). If the resulting equation was greater than 1, the ray was outside of the ellipsoid/rod. If the equation was less than or equal to 1, the ray was within or at the surface of the ellipsoid, respectively. Once it was determined that a ray had indeed struck a rod, an iterative scheme was used to determine the exact point of ray contact,

1) Evaluate equation (21) for the ray's position at the current time step, $(x, y, z)_i$. Set P1 equal to this solution
2) Evaluate equation (21) for the ray's position at the previous time step, $(x, y, z)_{i-1}$. Set P2 equal to this solution. Use the time step Δt, calculated from equation (24).
3) If |1-P1|<tol or |1-P2|<tol (tol=0.0001), then set point_collision equal to $(x,y,z)_i$, or $(x,y,z)_{i-1}$, and set dt_new equal to Δt or 0, respectively. Proceed to step 5).
4) If the solution was not found in step 3), then calculate
    a. Slope=(P2-P1)/ Δt
    b. dt_new=(1-P1)/Slope
    c. $(x, y, z)_{i-0.5} = (x, y, z)_{i-1}$ + V*dt_new, where V is the ray's velocity vector before collision.
    d. Evaluate equation (21) with $(x, y, z)_{i-0.5}$. Set P3 equal to this solution.
    e. If |1-P3|<tol, then proceed to step 5), and set point_collision equal to $(x, y, z)_{i-0.5}$.
    f. If e. failed to produce a value within the tolerance, then if P3<1, set P2=P3. Alternatively, if P3>1, set P1=P3 and set $(x, y, z)_{i-1} = (x, y, z)_{i-0.5}$.
    g. Return to step a)

5) Once point_collision has been determined, set dt_left = Δt - dt_new.
6) Evaluate equation (15) using point_collision. Set V equal to this solution.
7) Set $=(x, y, z)_i$= point_collision +V*dt_left

One now has the new reflected ray position and trajectory of the ray.

5.9 Simulation Exit Criteria

In order to determine when to stop the program from running, two limits were created such that the simulation ended if either limit was exceeded. The first limit sets the maximum runtime,

$$T = \Delta t/\xi. \tag{25}$$

In other words, the minimum time that it takes light to cross the entire microrod array's longest dimension was set as the maximum runtime. The maximum number of

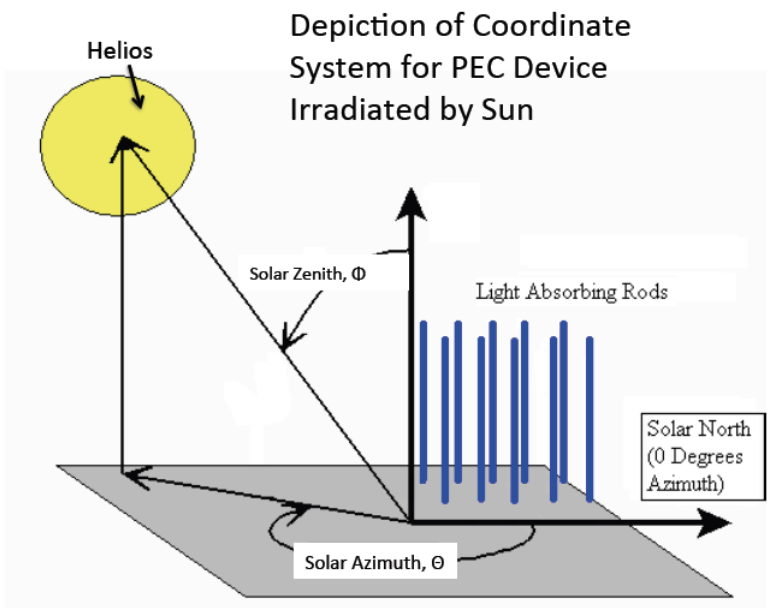

Figure 10: Depiction of solar zenith angle and solar azimuth.

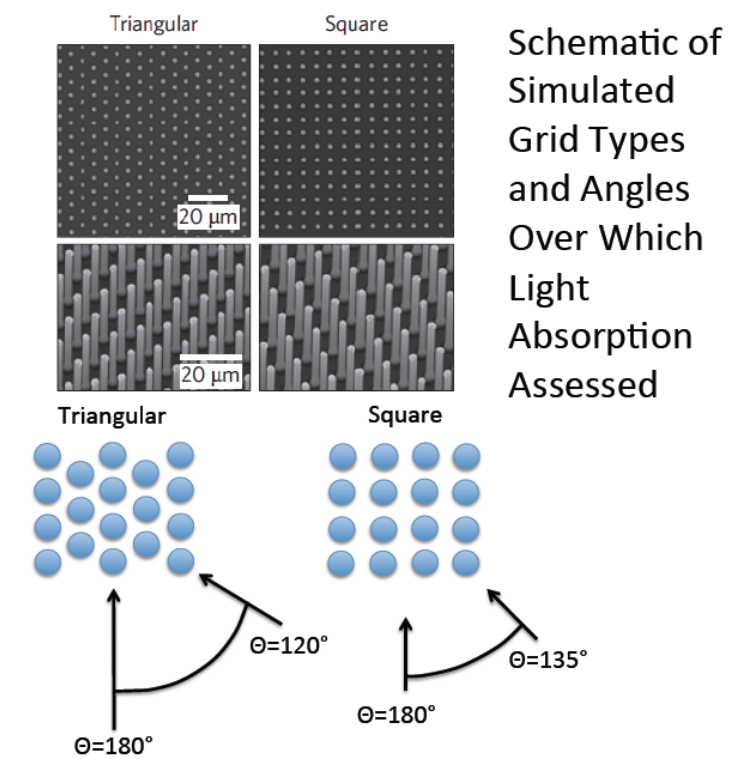

Figure 11: Images of grids used to make arrays and depiction of azimuth angles over which absorbance was modeled[27]. Note that scale in images on upper left is not indicative of that used in model.

[27] Photos of microrod arrays from Kelzenberg, 240.

iterations, i, that the program was allowed to run for is set at 30,000. Alternatively, the simulation ended if each of the rays was below or above the z-domain of the rods (0 to 100 μm).

5.10 Overall Computational Scheme

Having detailed the various computational subcomponents that were employed for the model, an overview of the program's execution steps are now given.

1) Generate a set of N rays, with initial propagation directions V_n, initial positions $(x, y, z)_n$ and initial magnitudes Io_n, where the subscript n denotes ray number ($1 \leq n \leq N$). Set t=0. Sum the total energy entering the system, $I_{Tot,O}$.
2) Increment the position of each ray using equation (23).
3) Check to see if each ray has encountered a rod using equation (21), as described above.
    a. If the ray has encountered a surface, locate the reflection location, calculate the reflected ray location and propagation direction, calculate the reflectivity and calculate the energy absorbed during reflection.
4) $t=t+\Delta t$
5) Check to see if the exit criteria are satisfied. If so, exit the simulation and sum the total energy of the rays, $I_{Tot,F}$. If not, return to step 1)
6) The total fraction of energy that is absorbed for a particular direction of incidence is $I_{Tot,F}/I_{Tot,O}$.

5.11 Implementation of a Genetic Algorithm to Find Optimal Grid Geometries

The author investigated using randomly generated microrod grids combined with a genetic algorithm (GA) to search for optimal microrod placement geometries. The program's execution steps and results are detailed here.

The first step in executing the GA was to generate 10 microrod grids with square dimensions of L = 0.5 mm. Each grid was subdivided into 625, 20 μm by 20 μm square sections. Then, 625 microrods were placed on each grid, with one rod per 20 μm by 20 μm square section. The location of each of the microrods' bases was chosen randomly within its respective 20 square μm section, and these sections were further randomly shifted relative to one another such that no two rods were within 4 μm of one another (to satisfy the criteria for utilizing ray tracing). All grids contained identical, 5 μm diameter, 100 μm tall rods. The AF of the grids was 4.91%. All rods were comprised of Ni and $SrTiO_3$ with a surrounding medium of pure water at 300 K and pH 7.0, and the outer coating of $SrTiO_3$ had the same thickness as that used above.

The absorbance of each grid was evaluated by running the ray tracing simulation as described above in sections 5.1-5.10. The incident angle of light was varied by sweeping Φ from 0° to 30° in 10° increments and θ from 135° to 180° in 15° increments. 1,000 incident rays were used. All other elements of the program adhered to the criteria set forth in sections 5.1-5.10. Once all simulations had completed, the best performing (highest average absorbance) designs were selected. Designs that most closely matched in terms of average absorbance were then paired, to form two "parents". The X- and Y-positions of each rod within the corresponding 20 μm square sections of each parent

were then randomly combined. This "mating" of X- and Y-positions was performed twice for each pair of parents, creating two "children" per parental pair. The parents and children were then augmented by a new crop of randomly generated grid geometries, such that the total "population" of grids equaled that initially generated. To finish a "generational" iteration, the program was used to again evaluate the absorbance of the children as well as new members of the array population. In total, ten generations of the GA were run to try to "evolve" an optimal design.

6. Results of Microrod Absorbance Simulations

6.1 Ray Tracing Simulation Results for Regular Grids

Results of the program simulations for regular grids are presented as surface plots below, in Figures 12-15. These figures represent the best (Figures 12 and 14) and worst (Figures 13 and 15) performing array designs for square and triangular grid patterns, respectively. Table 1 summarizes the simulation results for regular grids.

A square array always absorbed more energy on average than a triangular array of identical pitch. Table 1 shows that this was true across almost the entire range of zenith angles. The fact that the square array performed better for zenith angles between 0° and 45° is important because light entering the actual array would bend towards smaller zenith angles before making contact with the microrods. Each array exhibited the worst absorbance when the solar declination angle equaled 0°. This makes sense, as these rays did not have the proper initial trajectory to undergo multiple intra-rod

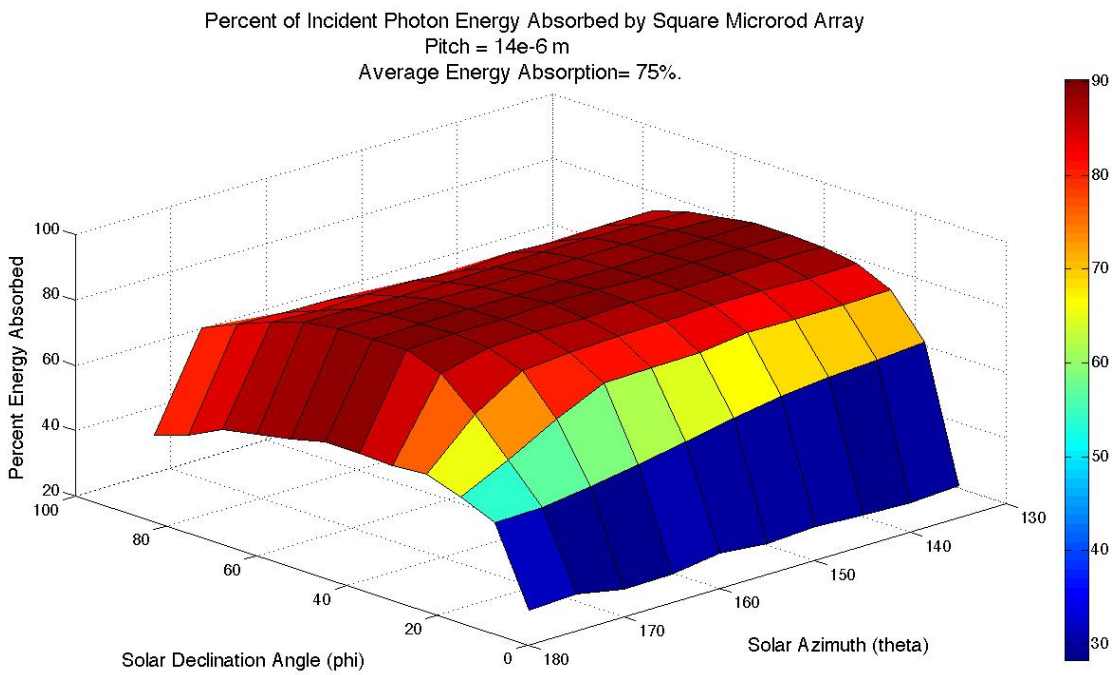

Figure 12: Profile of microrod array absorbance as a function of solar declination and azimuth, for a 14 μm pitch square array. This was the best performing design for square arrays.

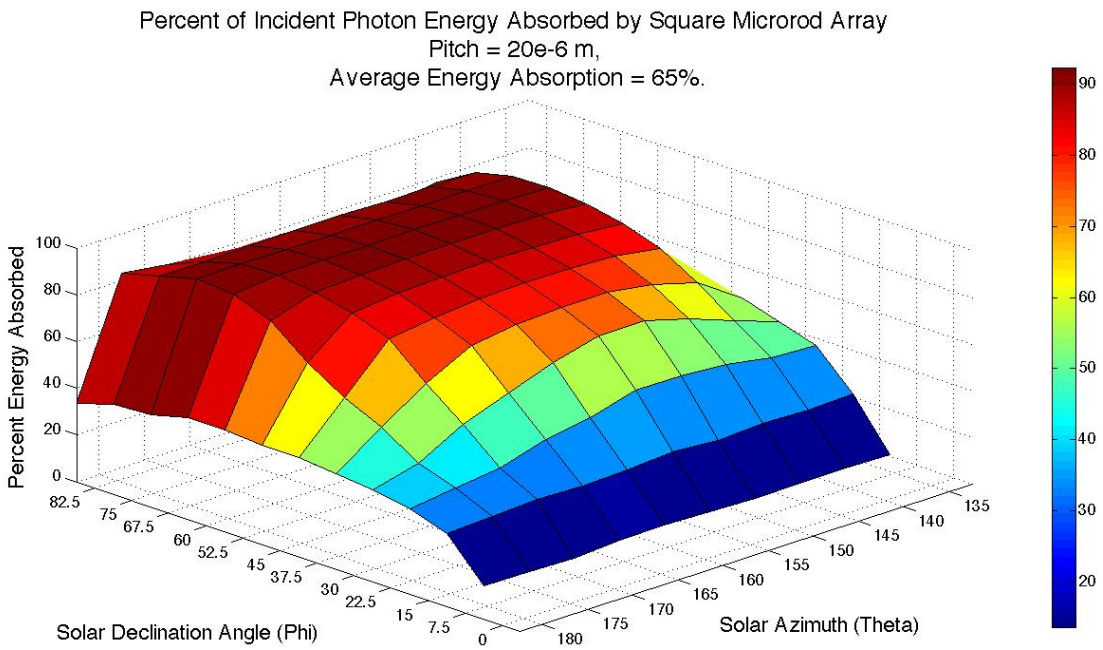

Figure 13: Profile of microrod array absorbance as a function of solar declination and azimuth, for a 20 μm pitch square array. This was the worst performing design for square arrays.

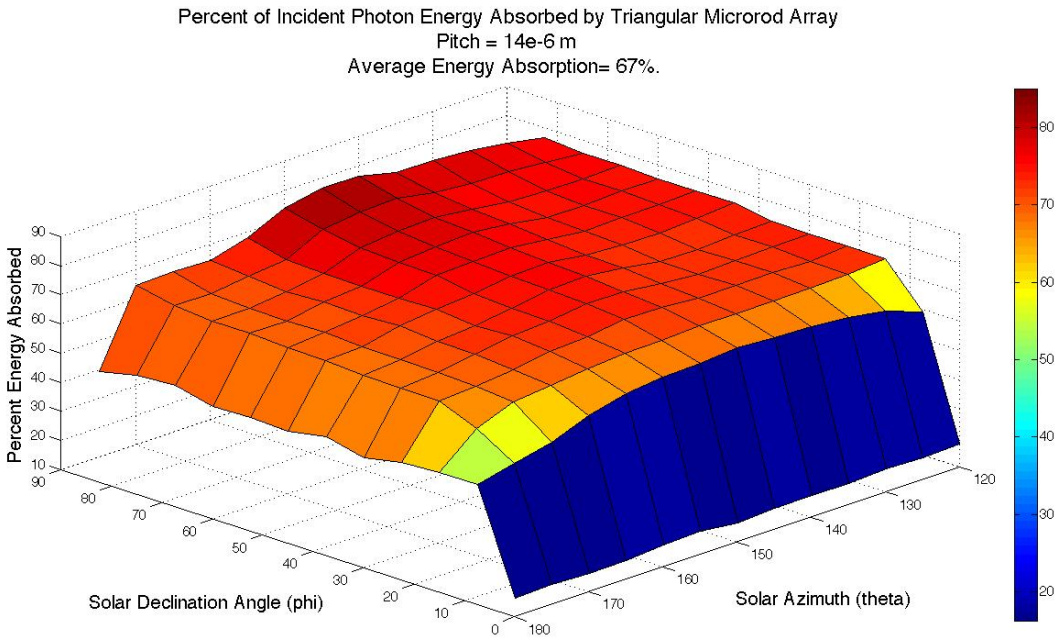

Figure 14: Profile of microrod array absorbance as a function of solar declination and azimuth, for a 14 μm pitch triangular array. This was the best performing design for triangular arrays.

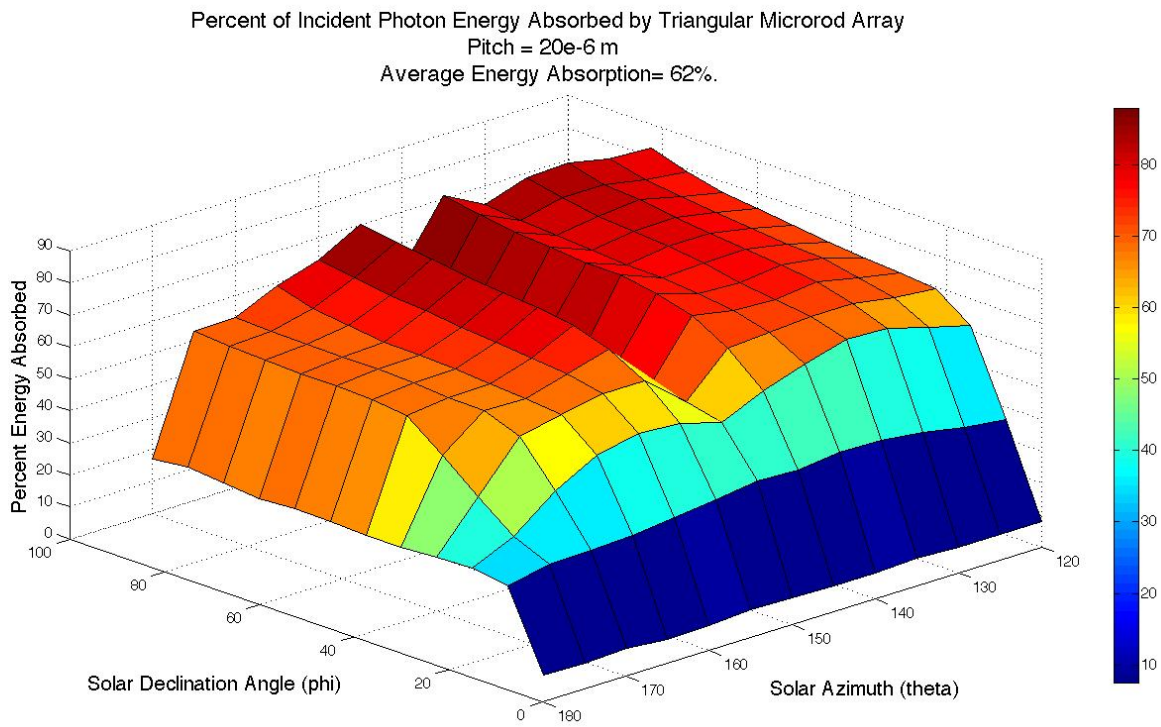

Figure 15: Profile of microrod array absorbance as a function of solar declination and azimuth, for a 20 μm pitch triangular array. This was the worst performing design for triangular arrays.

reflections unless they struck the edges of the top of a rod at certain locations. Both square and triangular arrays exhibited absorbance "dead spots" as the azimuth of the light was varied. These occurred at points where incoming light traveled in a ballistic manner through the array, parallel to the rows of rods, regardless of zenith angle. For square arrays, this occurred when the azimuth equaled 180°, and to a lesser extent at 135°. For triangular arrays, these low absorbance regions occurred when the azimuth equaled 180° and, again to a lesser extent at 120°. Curiously, there was a dip in absorbance when the azimuth equaled 145° for triangular arrays that only was evident for some larger pitch values. As the pitch increased, the solar zenith angle at which optimum absorbance occurred increased, though this effect was more obvious for square arrays.

Though triangular arrays exhibited worse performance than square arrays in the examined range of pitch, Table 1 shows that the decline in performance of triangular arrays was less steep than for square arrays as pitch was increased. From a materials standpoint, a square array has the advantage of having a lower AF than an equilateral triangular array of the same pitch. A square array with identical rod dimensions would contain less active material than a triangular array, reducing material cost.

6.2 Ray Tracing Simulation Results for Random Grids

The author was unable to find much difference in the performance of any of the random grids generated. A notable feature of all random grids was that their absorbance performance was nearly isotropic with respect to θ (see Figure 16). This is a logical

Average Absorption, Triangular Arrays

Pitch (µm	Solar Zenith Angle (Φ) 0	7.5	15	22.5	30	37.5	45	52.5	60	67.5	75	82.5	Total Average Absorption	Average Absorption for 0< Φ < 45
14	17.2%	62.7%	68.4%	69.9%	70.3%	70.7%	71.4%	72.0%	72.4%	73.0%	74.3%	76.7%	**66.6%**	**61.5%**
15	15.3%	58.8%	67.4%	69.6%	70.3%	70.8%	71.2%	72.0%	72.7%	73.4%	74.7%	77.0%	**66.1%**	**60.5%**
16	13.1%	54.7%	66.1%	69.1%	70.3%	71.0%	71.5%	72.1%	72.7%	73.6%	74.7%	77.0%	**65.5%**	**59.4%**
17	11.5%	49.9%	64.5%	68.1%	69.8%	70.8%	71.5%	71.8%	72.6%	73.5%	74.6%	76.6%	**64.6%**	**58.0%**
18	10.3%	45.8%	62.5%	66.9%	69.3%	70.5%	71.2%	71.8%	72.5%	73.3%	74.6%	76.7%	**63.8%**	**56.6%**
19	9.2%	41.9%	60.0%	65.6%	68.4%	70.1%	71.0%	71.7%	72.2%	73.0%	74.0%	76.5%	**62.8%**	**55.2%**
20	8.3%	38.2%	57.7%	64.3%	67.5%	69.5%	70.6%	71.4%	72.0%	73.1%	74.4%	76.4%	**62.0%**	**53.7%**

Average Absorption, Square Arrays

Pitch (µm	Solar Zenith Angle (Φ) 0	7.5	15	22.5	30	37.5	45	52.5	60	67.5	75	82.5	Total Average Absorption	Average Absorption for 0< Φ < 45
14	29.8%	62.3%	77.0%	83.3%	86.0%	86.7%	86.4%	85.5%	83.8%	80.3%	74.4%	65.4%	**75.1%**	**73.1%**
15	26.1%	56.2%	71.8%	79.8%	84.0%	86.2%	86.8%	86.3%	84.9%	81.9%	76.4%	66.0%	**73.9%**	**70.1%**
16	22.7%	50.1%	67.3%	76.3%	81.7%	84.5%	85.9%	85.7%	84.6%	82.2%	77.0%	66.8%	**72.1%**	**66.9%**
17	20.0%	45.3%	61.6%	72.3%	78.6%	82.7%	85.0%	85.5%	84.6%	82.5%	77.7%	67.3%	**70.3%**	**63.7%**
18	18.7%	41.2%	57.0%	68.3%	75.5%	80.2%	83.3%	84.8%	84.6%	83.0%	78.7%	68.4%	**68.6%**	**60.6%**
19	16.7%	37.3%	52.4%	63.7%	71.7%	77.7%	81.9%	84.0%	84.5%	83.3%	78.8%	69.2%	**66.8%**	**57.3%**
20	14.3%	33.3%	48.2%	60.1%	68.9%	75.0%	79.5%	83.0%	84.0%	83.1%	79.5%	70.2%	**64.9%**	**54.2%**

Table 1: Absorbance for all simulated solar zenith angles averaged across all simulated solar azimuth angles, for square and triangular arrays.

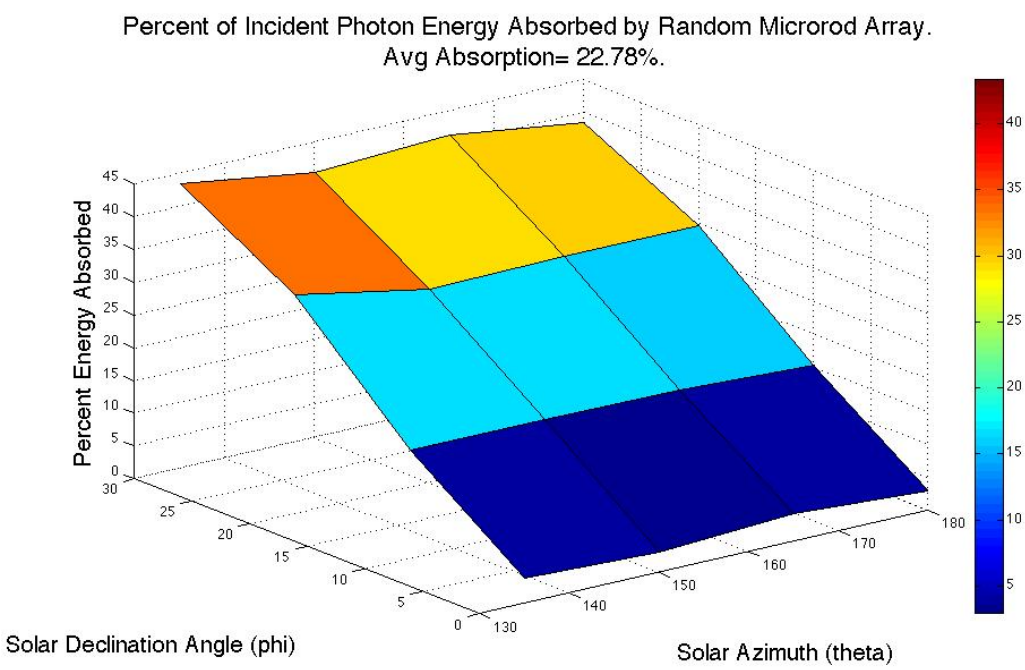

Figure 16: Profile of microrod array absorbance as a function of solar declination and azimuth for the best randomly generated, 4.91% AF rod grid containing 5 µm diameter, 100 µm tall rods

conclusion, as none of the behavior of ballistic rays detailed in section 6.1 could be observed if there was not a regular grid design. Additionally, within the narrower scope of incident angles investigated relative to those detailed above, the randomly generated grid had a slightly higher average absorbance than a square grid of the same AF (see Figure 17.)

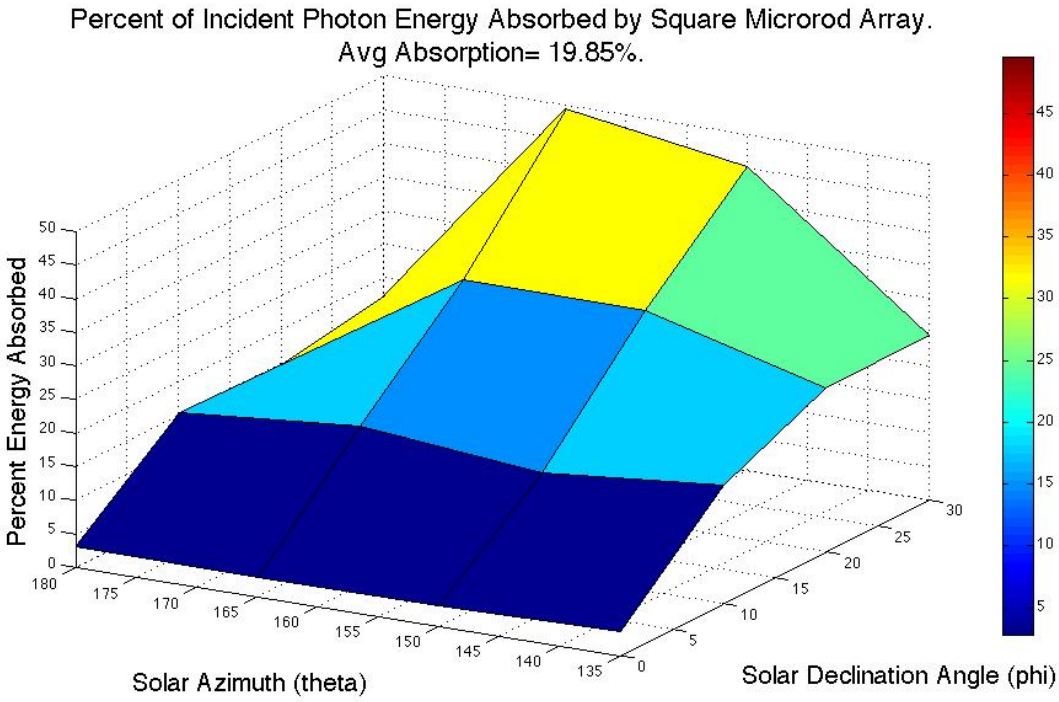

Figure 17: Profile of microrod array absorbance as a function of solar declination and azimuth for a square, 4.91% AF rod grid containing 5 μm diameter, 100 μm tall rods

6.3 Results from Other Investigators

There have been prior attempts to experimentally characterize the absorbance of Si microwire arrays by Kelzenberg et al. These investigators performed measurements of the absorbance of an array of 67 μm long microwires as a function of angle of incidence using an integrating sphere. The diameter of the microwires is not explicitly given in Kelzenberg et al's paper, but the images in Figure 11 show these rods. It is obvious that they were significantly less than 10 μm in diameter. It is stated that the AF of the modeled array was 4.2%. This is below the AF of arrays that were simulated by the author in section 6.1 (the lowest AF was 19.6% and 22.6% for grid arrays, respectively), but close to that in section 6.2.

The results of absorbance versus angle of incidence indicate that the absorbance profiles generated in this analysis are qualitatively reasonable, primarily in the location of "dead spots" in the absorbance of triangular and square grid patterns when the azimuth was varied, as well as the lack thereof for random grid patterns. Additionally, the low absorbance at incidence from small solar zenith angles was also demonstrated. However, the maximum absorbance demonstrated by Kelzenberg et al (~90%) is significantly higher than that demonstrated here for grids of a similar AF. It is difficult to

draw quantitative comparisons between these separate analyses because the microrod geometries and PV band gaps employed in the two investigations are quite different.

7. Bubbles in a PEC Device

7.1 The Importance of Light Interactions with Bubbles in a PEC Device

Thus far, the simulations have focused solely on a PEC device's light absorber, idealized as microrods immersed in water. In operation, bubbles of oxygen and hydrogen will form at the device's anode and cathode. These bubbles will grow as more gas molecules are produced and, if the anode and cathode's orientation with respect to gravity permits, eventually be driven off of their surfaces into the electrolyte by buoyant forces. The author and his colleagues have experimentally observed this phenomenon of surface bubble growth. Figure 18 below is a photograph of an amorphous silicon sheet of PV material immersed in electrolyte. It was under illumination, and oxygen bubbles evolving on the surface of a thin film of IrO_2 catalyst that coats the PV sheet are visible.

The bubbles in Figure 18 appear white because they were reflecting the incident light. Any light reflected away from the microrod grid will reduce the device's surface current density and efficiency. The microrod grid in the PEC simulated in this analysis was arranged as a flat plane of vertically oriented rods. The author has therefore simulated how bubbles on the surface of a flat plane (i.e. the tops of the microrod grid) scattered incident light before it entered the microrod grid's spatial domain to try to estimate the resultant reduction in energy available to generate solar fuels.

The reflectance of light incident on bubbles of oxygen can be calculated using equations (19) above, because oxygen and water are effectively dielectrics for optical wavelengths. Figure 19 gives a plot of reflectance versus incident angle for 385 nm light traveling from water to oxygen. The plot indicates that θ_c is about 49° for visible light (the exact angle varies slightly with wavelength), meaning that all light incident from water to an oxygen bubble at angles greater than θ_c will be completely reflected. This explains the reflective nature of the bubble coating seen in Figure 18.

7.2 The Physics of Bubbles

When bubbles form on a planar surface, their overall shape is dictated by buoyancy as well as the interfacial energies between the substrate, surrounding fluid and the fluid within the bubble. The overall force balance between these interfacial energies for a sessile droplet of water on an infinitely smooth solid surface surrounded by gas gives rise to Young's equation, from which one can determine the contact angle $\theta_{contact}$,

$$\Upsilon_{sg} - \Upsilon_{sl} - \cos(\theta_{contact})\,\Upsilon_{lg} = 0, \tag{26}$$

where Υ_{sg} is the interfacial energy between the solid and gas phases, Υ_{lg} is the interfacial energy between the liquid and gas phases, and Υ_{sl} is the interfacial energy between the solid and liquid phases. By convention, $\theta_{contact}$ is measured from the substrate through the liquid (see Figure 20). For droplets of water, hydrophilic surfaces are those with $\theta_{contact}$ less than 90° and hydrophobic substances are those with $\theta_{contact}$ greater than 90° (e.g. a bead of water on a waxy surface, surrounded by air).

It was necessary to get an idea of the bubble size at the point where buoyancy initiated detachment. This placed an upper bound on the size of bubbles to simulate, which dictated what method to use to simulate the interaction between bubbles and light. To calculate this bound, it was assumed that hemispherical bubbles of air grew upon a flat surface, surrounded by water. Using properties of air instead of

Figure 18: Oxygen bubbles evolving on a sheet of amorphous silicon[28].

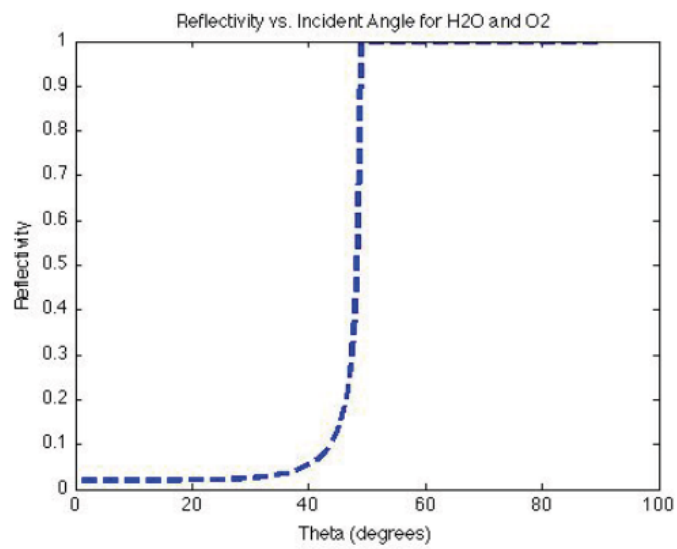

Figure 19: A Graph of Reflectivity vs. Incident Angle for light incident from water to oxygen.

oxygen was deemed reasonable owing to the high concentration of oxygen in air. The force adhering this bubble to the surface was calculated as

$$F_S = \sigma * 2\pi R, \tag{27}$$

where σ is the surface tension between water and air at 300 K and R is the bubble radius. The buoyant force for this hemispherical bubble was calculated as

$$F_B = (\rho_{H2O} - \rho_{O2})\frac{2\pi}{3}R^3 g, \tag{27}$$

where ρ is the fluid density and g is the gravitational constant. Equating these two forces and solving for R gave a bubble radius of approximately 4.7 mm at detachment from a horizontal surface. Based upon the author's experimental observations, this is a reasonable estimate.

[28] Photo credit: William West, California Institute of Technology

7.3 Methods for Modeling Light Interactions with Bubbles

There are multiple methods at one's disposal to model light interactions with a sphere such as a bubble; three methods will be discussed here. Lorenz Mie Theorem (LMT) provides an exact solution to the scattering of light by a homogeneous dielectric sphere in free space, regardless of its size relative to the incident light's wavelength. However, the LMT is computationally expensive[29]. The Rayleigh approximation and the geometric optics approach (GOA) are approximate methods to use when the size parameter is very small or very large. The size parameter is defined as

$$\xi = \pi D/\lambda_m, \tag{28}$$

where λ_m is the wavelength of light in the sphere and D is the sphere diameter. For $\xi < 0.3$, the Rayleigh approximation is applicable, and for $\xi > 25$, the geometric approximation can be utilized[30]. Given the bubble radius calculated above and the 385 nm light simulated in this analysis, the size parameter is approximately 38,000. Obviously, then, one should use the GOA. Simulating longer wavelength light within the visible and infrared spectrums is also possible given the size of ξ calculated above. The large size of ξ also obviated the need to reduce the error resulting from the approximate nature of the calculation given above for the bubble radius at the point of detachment.

When light interacts with a dielectric sphere, it is reflected by the sphere, transmitted through it and diffracted around its edges. The output of the GOA is a directionally varying intensity of the scattered light. The GOA utilizes ray tracing to model the reflected and transmitted trajectories of light. The GOA also calculates the scattering of light by diffraction and the interference pattern of light that is scattered by the sphere onto an arbitrary surface external to the sphere. The diffracted component is calculated as,

$$S(\xi, \psi) = \xi^2 \frac{J1(\xi \sin(\psi))}{\xi \sin(\xi)}, \tag{29}$$

where ξ is the size parameter, J1 is a first order Bessel function and ψ is the scattered angle (see Figure 20). There are multiple relations for calculating the interference pattern that are not listed here for the sake of brevity. For more information on these terms, the reader is directed to the work of de Hulst[31] and Yu et al[32].

The author implemented a form of the GOA that relied primarily on the ray tracing framework set forth earlier in this analysis. The model did not include terms for

---

[29] John Howell, Robert Siegel and M. Pinar Mengüç. Thermal Radiation Heat Transfer. 5th Edition. New York: CRC Press, 2010. 747.

[30] Howell, 755, 764.

[31] Van de Hulst, H.C. (Ed.) Light scattering by small particles. New York: John Wiley & Sons, 1957.

[32] Yu et al. "Geometrical optics approximation of light scattering by large air bubbles", Particuology 6 (2008) 340-346.

the diffraction or interference of light. It was reasoned that the effect of diffraction is small for bubbles of this large scale, as are the deleterious effects of interference on energy harvesting by a PEC device.

8. Computational Scheme for Modeling Light Scattering by Oxygen Bubbles

8.1 Ambient Environment

As before, the surrounding media around the bubbles was modeled to be pure, pH 7.0 water at 300 K and the simulated wavelength was 385 nm. The optical properties of oxygen were also those measured at 300 K and 1 atmosphere, though strictly speaking the pressure within the bubbles would be significantly higher than 1 atmosphere[33]. The type of surface upon which the bubbles rested was not modeled, other than as the lower Z-bound of the simulated domain.

8.2 Simulation of Bubble Geometry

Placing bubbles upon a flat surface was accomplished by first setting the maximum bubble radius, R_{Max} (as calculated above). The minimum bubble radius in the simulation, R_{Min} was then chosen as $1/10^{th}$ of the maximum radius. As such, the smallest bubble had $1/100^{th}$ the AF of the largest bubble. Smaller values for R_{Min} can be chosen, but little effect was noted by doing so. A minimum clearance was then set such that no two bubbles were closer than $20 * \lambda_m$, out of consideration for the applicability for using ray tracing, and for idealizing the bubbles as independent scatterers[34]. The maximum number of bubbles, $N_{Bubbles,Max}$ was set at 2,000, and the radius of each bubble was randomly generated as follows:

$$R_{Bubble,i} = R_{Min} + (R_{Max} - R_{Min}) * \mathrm{rand}(1), \tag{30}$$

where rand(1) is a single randomly generated number from 0 to 1. The contact angle was specified (without using equation (26)), and the height of the centroid of each sphere relative to the plane they rest on was calculated as

$$\begin{aligned} H_{Centroid} &= R_{Bubble,i} * \cos(\theta_{contact}) \text{ or} \\ H_{Centroid} &= -R_{Bubble,i} * \cos(180 - \theta_{contact}), \end{aligned} \tag{31}$$

depending upon if $\theta_{contact}$ was less than or greater than 90°, respectively. The X- and Y-coordinates of the bubble's centroid were then calculated randomly using the same method as that employed in equation (30), with the bounds on the X- and Y-extents of the bubble coated surface set as 0 to 5 cm. Then, the bubbles were inserted into the domains sequentially. As each bubble was inserted, its proximity to other bubbles was calculated, and if any bubbles that were already on the surface were closer than $20 * \lambda_m$

[33] Van P. Carey. Liquid Vapor Phase Change Phenomena: An Introduction to the Thermophysics of Vaporization and Condensation Processes in Heat Transfer Equipment, 2nd Edition. New York: Taylor Francis Group, 2008. 46.
[34] Howell, 781.

to that being inserted, then new X- and Y-coordinates of the candidate bubble were randomly generated. Each bubble could be placed in a different location up to 500 times before the bubble was excluded from the simulation. After each bubble was placed, the total AF of bubbles was calculated. The program stopped placing bubbles on the surface when 50% AF was exceeded. As a result, the total number of bubbles actually in the simulation, $N_{Bubbles}$, was always lower than $N_{Bubbles,Max}$. Finally, the program iterated through each of the bubbles placed upon the surface and tabulated all the bubbles within 2.5 times the maximum bubble radius in the simulation. This binning of neighboring bubbles was done to speed up calculations in the main simulation.

8.3 Setting and Tracking Ray Position and Energy as a Function of time

In order to increment ray position at each time step, the explicit scheme detailed in section 5.6 was used, with some changes. Δt was calculated as

$$\Delta t = \frac{\min\left(R_{Min}, 20*\lambda_m\right)}{\left|V_{\text{Light in Medium}}\right|*10}, \tag{32}$$

The initial X- and Y-domain of the rays was a square region extending for 40% of the X- and Y-extents of the simulated bubble domain, centered at X=2.5 cm and Y=2.5 cm. The initial Z-position of the rays was 1.01*H, where H was the Z-location of the highest point of the largest bubble on the surface. An evenly spaced grid of rays, all at the same Z-position, was placed within the X- and Y-bounds of the subdomain for the rays. The ray spacing was made even rather than random to aid repeatability. For all simulations, N rays = 900. Adding more rays than this into the simulation did not greatly affect results.

The typical interaction of a ray with a bubble can be seen in Figure 20. Unless a ray is totally reflected (it strikes the exterior surface of the bubble at an angle greater than θ_c), each time a ray interacts with the oxygen-water interface, a portion of the ray is reflected and a portion is transmitted through. As both substances were assumed to be dielectric in the simulation, none of the incident light was modeled as absorbed in this process. For each reflection that occurred, the energy of the ray that was reflected was I_o*R, and that which was transmitted was I_o*(1-R). R was calculated using equations (19) and I_o was the incident ray energy.

Each time a reflection event occurred, the number of rays increased by one. In order to limit the total number of rays in the simulation, a criteria was set such that if an individual ray contained less than 0.1% of the energy that each ray initially contained before the simulation began, it was removed from the simulation. The initial amount of energy was arbitrary, and was equal for all rays. If a ray was removed, the total energy it contained was logged so that the loss in total energy within the simulation was accounted and corrected for.

8.4 Setting Initial Ray Propagation Direction

In order to simulate a wide range of possible incident angles, the range of Φ was varied from 0° to 45°, in 7.5° increments. As stated before, it can be shown that, owing to the index of refraction of water, that light entering the device will bend towards Φ=0°, with the maximum transmitted zenith angle roughly equaling 49° (see equation (17)). Hence,

this was a reasonable range of azimuth angles to investigate. Owing to the random nature of the bubble placement and radius, and the symmetrical nature of the bubbles, it was reasoned that the overall optical response of light interacting with the bubbles would be, roughly speaking, isotropic with respect to θ. Hence, θ was set to 0° for all simulations, and multiple simulations were run to ascertain if the optical performance of multiple randomly generated sets of bubbles were comparable.

8.5 Modeling Reflection Locations from Bubbles

The method employed to find the location of rays striking the surface was identical to that described in section 5.8.

8.6 Simulation Exit Criteria

The simulation was set to run for a maximum of 20,000 time steps, until the energy within the simulation dropped below 0.5% of the total energy entering the simulation, or until all rays exited the bubbles' simulation domain.

8.7 Overall Computational Scheme

Having detailed the various computational subcomponents that were employed for the model, an overview of the program's execution steps is now given.

1) Generate a set of 900 rays, with initial propagation directions V_n, initial positions $(x, y, z)_n$ and initial magnitudes I_o, where the subscript n denotes ray number ($1 \leq n \leq N$). Set t=0. Sum the total energy entering the system, $I_{Tot,O}$.
2) Increment the position of each ray using equation (23).
3) Check to see if each ray has encountered a bubble using equation (21), as described above (using P=2 instead of 70).
    a. If the ray has encountered a surface, locate the reflection location, calculate the reflected/transmitted ray location and propagation direction, calculate the reflectivity and calculate the energy allocated to the reflected and transmitted rays.
4) t=t+Δt
5) Check to see if the exit criteria are satisfied. If so, exit the simulation and sum the total energy of the rays that exit the domain through the top of the Z-domain (1.01*H), $I_{Tot,R}$. If not, return to step 1)
6) The total fraction of energy that is reflected away from the absorber for a particular direction of incidence is $I_{Tot,R}/I_{Tot,O}$.

9. Results of Bubble Reflectance Simulations

9.1 Results for $\theta_{contact} = 45°$

The amount of energy reflected back from the bubble covered surface with $\theta_{contact} = 45°$ as a function of Φ is depicted in Figure 21. 4 simulations were performed, each on a different randomly generated array of bubbles. The simulations showed that the reflectivity was at or near a minimum for Φ=0°, and increased (though not always

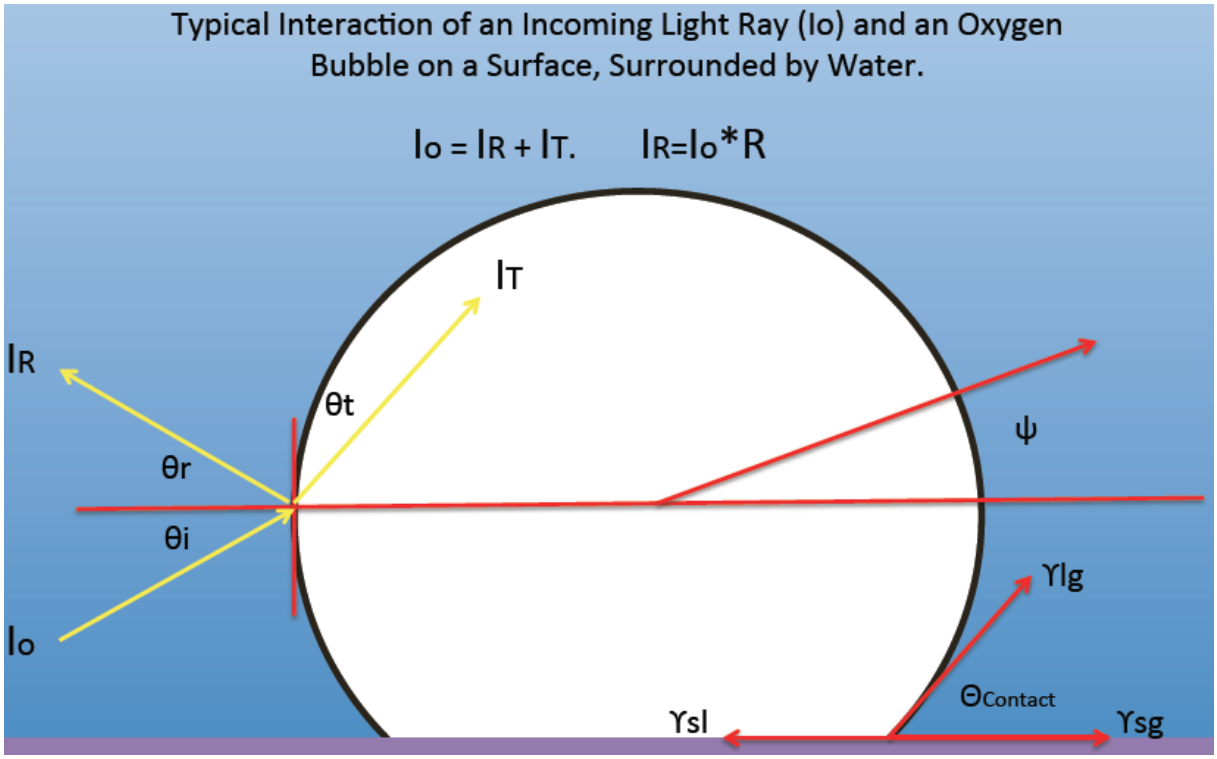

Figure 20: Depiction of various bubble related nomenclature and sample ray reflection.

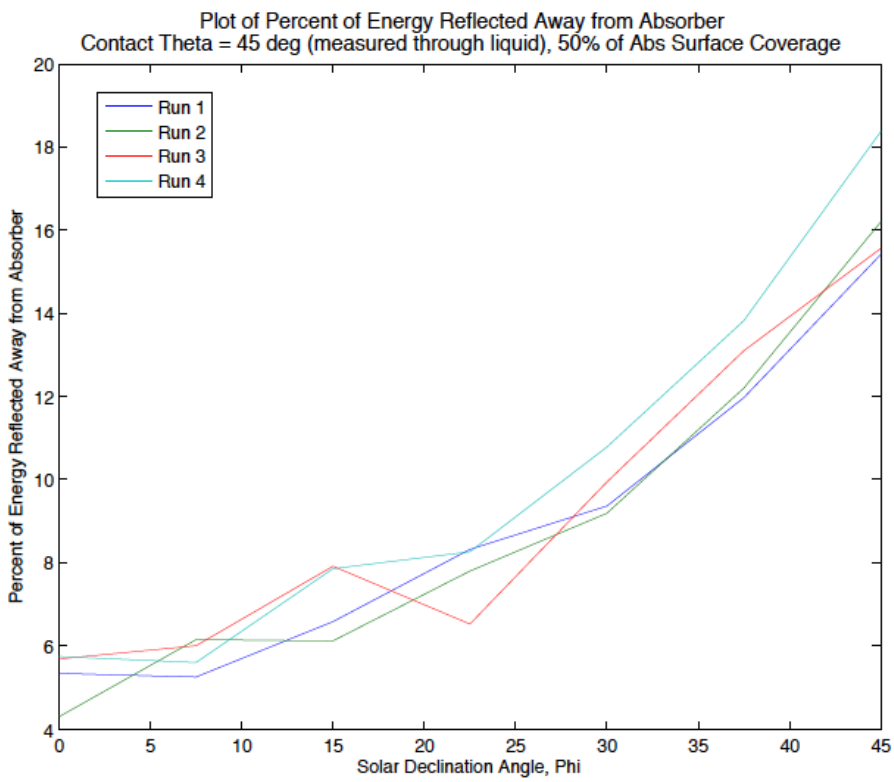

Figure 21: Results for simulations of bubbles on an absorber surface with 50% AF and a 45° contact angle.

monotonically) as the zenith angle increased. The overall range of reflectivity was from about 4% to 18%. These results make sense, for as the zenith angle increased, the first reflection that a ray made with a bubble was closer to θ_c, thus the net reflectivity increased (see Figure 19). There was generally good agreement between the individual runs.

Figure 22 shows the trajectories at which light entered the absorber for Φ=45°, and Figure 23 shows the trajectories at which light was reflected off the bubbles, away from the absorber for Φ=45°. These results were for a single bubble array. Figure 22 demonstrates that, at least for this particular incident angle, about 34% of the light still entered the absorber at roughly the same trajectory to that at which it entered the PEC device, and the rest was very evenly distributed across all trajectories. On the contrary, the reflected energy was scattered in a more random fashion with respect to Φ. These trends were seen in other simulations run by the author. In a sense, this is unfortunate, for it would be advantageous if all the light that headed towards the absorber was scattered at high zenith angles to enhance absorbance by the microrod grid. In general, these results show that bubbles will cause a noticeable drop in PEC device output, owing to the reduction in insolation that reaches the microrod array.

9.2 Results for $\theta_{contact} = 135°$

The amount of energy reflected back from the bubble covered surface with $\theta_{contact} = 135°$ as a function of Φ is depicted in Figure 24. 4 simulations were performed, each on a different randomly generated array of bubbles. The results were largely similar to those in section 9.1. The overall range of reflectivity was from about 2% to 20%. The larger value of $\theta_{contact}$ meant that the light encountered an interface that was closer to the flat

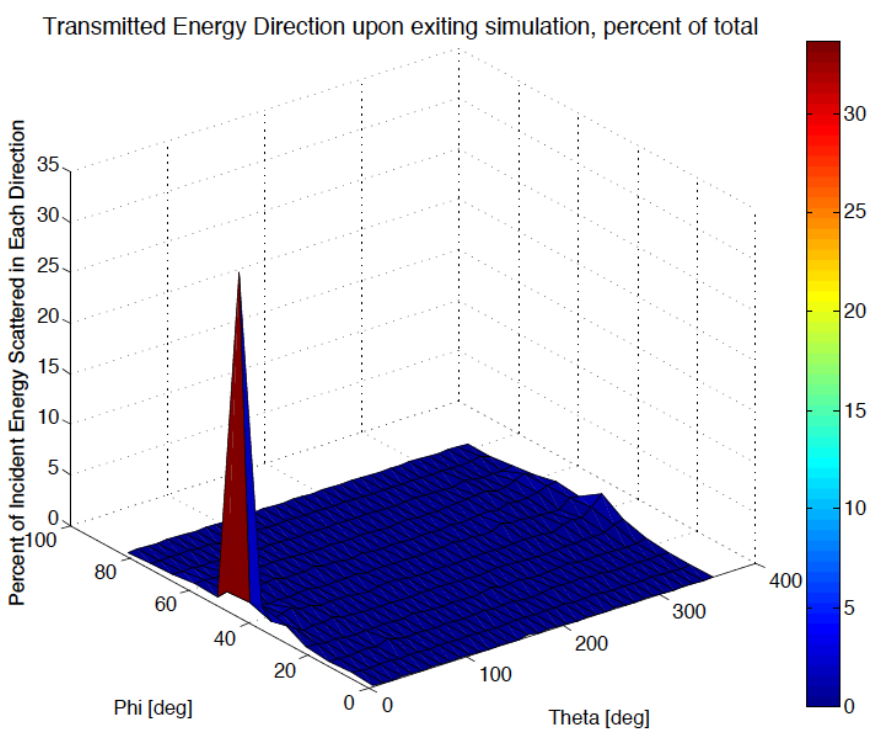

Figure 22: Plot of transmitted energy direction for an absorber surface covered with bubbles having a 45° contact angle.

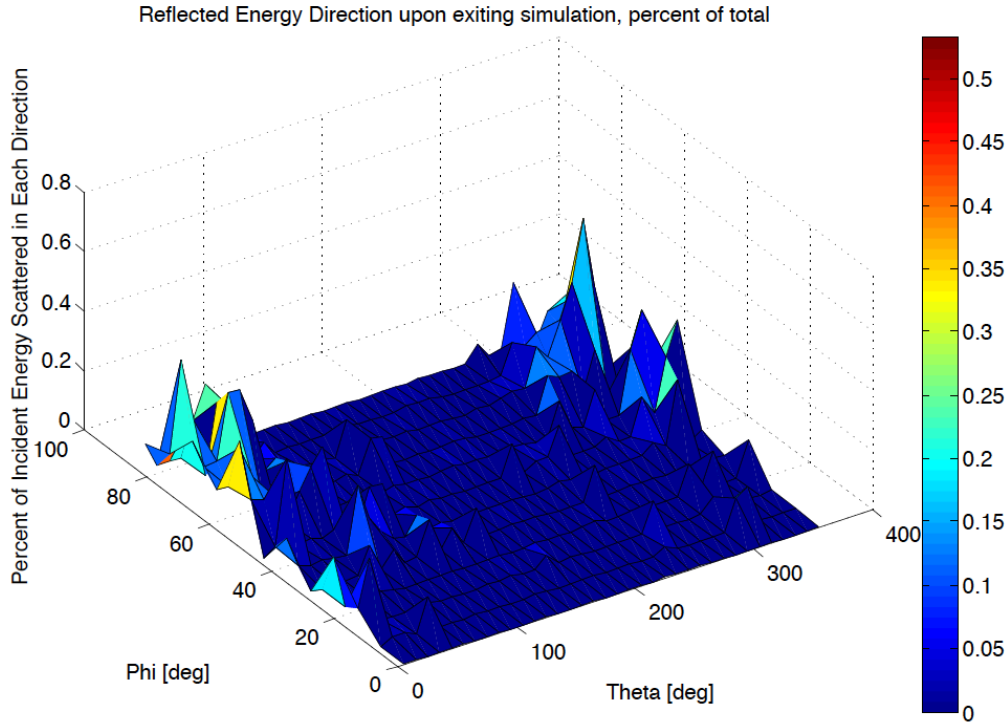

Figure 23: Plot of reflected energy direction for an absorber surface covered with bubbles having a 45° contact angle.

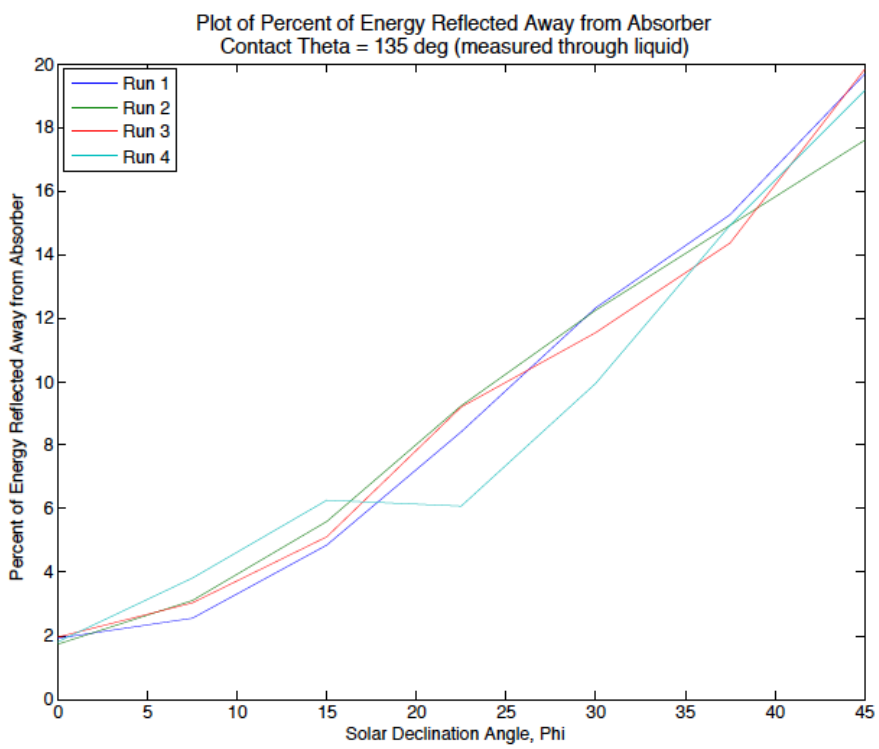

Figure 24: Results for simulations of bubbles on an absorber surface with 50% AF and a 135° contact angle.

interface modeled in Figure 19, which probably explains why there was a greater span in reflectivity over the investigated range of Φ. Due to buoyancy, it is unlikely that the actual bubbles will have this morphology, but it was simulated the sake of completeness.

10. Future Modeling and Experimental Work

10.1 Advantages of Using a Maxwell Equation Solving Optical Model that Simulates Microrods

There are a number of different ways in which the use of ray tracing to model microrod arrays is advantageous, but there are others in which it is problematic. In order to better characterize the microrod array, ray tracing will ultimately have to be replaced with an approach that uses physical optics, or some other approach that solves Maxwell's equations. The ways in which this will improve the model are presented below.

Surface catalysts on the microrods were not included in the ray tracing model. They were not incorporated because they would have been too small for ray tracing to accurately model. The size of catalyst sites was not precisely known at the time of writing, but they will likely be smaller than the rods themselves in order to not cover the entire rod surface. The presence of these catalysts may actually improve the predicted absorbance of the array, or at least not degrade it significantly. Other research has concluded that light scattering particles placed in the void space between microrods, as well as on their surface can enhance absorbance by randomizing the direction of light propagation through the rod array. This is especially helpful when the solar zenith angle, Φ, of the incident light is small[35]. Use of a physical optics will allow accurate simulation of light's interactions with these catalysts.

The dimensions of the rods modeled by the author were dictated by the array fabrication methods envisioned by the author's colleagues. It is very possible that other fabrication methods will be employed. The 10 μm diameter of the rods, as well as the pitch between the rods could shrink to below the threshold of ray tracing. Also, even apart from the catalysts, other rod geometries that involve features smaller than the ray optic limit may be introduced. These factors favor the flexibility of physical optics based simulations.

At the time of writing, the author's colleagues wished to build a PEC device prototype that functioned as a demonstration and debugging model. Ultimately, however, lower band gap materials (likely arranged in a multi-junction cell) will be employed to increase efficiency. If a single-junction cell with an optimal band gap of 2 eV is developed that can withstand the environment in a PEC device, the upper limit of wavelengths of interest will increase to approximately 620 nm. Even if the microrod dimensions do not change, the limit of ray optics may be exceeded through the inclusion of longer wavelength, lower frequency light in simulations.

[35] Kelzenberg, 241.

10.2 Experimentally Measuring Bubble Reflectance

The author plans to experimentally measure the reflectance of a surface evolving bubbles of oxygen to determine the validity of this model. The experimental work will also provide a better estimate as to the distribution of radii, contact angle and total AF of bubbles. The extent to which the incoming light is reflected away from the surface upon which bubbles evolve will determine whether or not to continue to improve the model by adding in extra features of a full GOA simulation, or focus on other work.

10.3 Add Bubbles in Other Locations

When operating, a number of bubbles will be rising in the column of electrolyte at any moment. Other gas bubbles will rest wherever they collect before extraction from the PEC device. Modeling the effect of more bubbles in the electrolyte will be an important step to reflecting the true behavior of this device. The results will likely indicate further reductions in the influx of light to the PV absorber.

10.4 Incorporate the Effects of Temperature Rise into the Model

The overall efficiency of any PEC device will be low enough that, when deployed in an area with high insolation, the device will get quite hot. The change in temperature has multiple effects. The solubility and surface tension of the electrolytes as well as the chemical reaction rates will change from the nominal values incorporated into this model and others generated by the author's colleagues. It is therefore important to determine the overall temperature rise of a deployed device, and to include temperature-varying properties of the electrolyte this model.

11. Conclusion

Ray tracing was used to search for the geometry of PV microrod arrays that produces maximum absorbance for 10 μm diameter, 100 μm tall rods made of $SrTiO_3$ and Ni. It was found that a pitch of 14 μm yielded the best absorbance for square grids and a pitch of 14 μm yielded the best absorbance for triangular grids. The square grids exhibited higher average absorbance than triangular grids. Random grids with 5 μm diameter, 100 μm tall rods exhibited slightly better absorption than square grids with the same rod dimensions, but no clearly superior design could be determined using a genetic algorithm. The presence of bubbles on the absorber surface will reflect significant amounts of energy away, reducing device output.

12. Acknowledgments

The author would like to thank Tarek Zohdi and Karl Walczak for their guidance and encouragement. This material is based upon work performed at the Joint Center for Artificial Photosynthesis, a DOE Energy Innovation Hub, supported through the Office of Science of the U.S. Department of Energy under Award Number DE-SC0004993. This work was supported by the Director, Office of Science, Office of Basic Energy Sciences, of the U.S. Department of Energy under Contract No. DE-AC02-05CH11231.

13. References

Almeida, B.G. et al. "Determination of infrared optical parameters of $SrTiO_3$ thin films from the reflectivity spectrum," *Thin Solid Films* 513 (2006), 275-282.

Abe, Ryu. "Recent Progress on photocatalytic and photoelectrochemical water splitting under visible light irradiation," *Journal of Photochemistry and Photobiology C: Photochemistry Reviews* 11 (2010) 179-209

Araujo, Gerardo and Antonio Martí. "Absolute limiting efficiencies for photovoltaic energy conversion," *Solar Energy Materials and Solar Cells* 33 (1994) 213-240.

Bak, T. et al. "Photo-electrochemical hydrogen generation from water using solar energy. Materials-related aspects," *International Journal of Hydrogen Energy* 27 (2002) 991-1022.

Cardona, Manuel. "Optical Properties and Band Structure of SrTiO3 and BaTiO3," *Physical Review* 140 (1965) A651-A655.

Carey, Van P. Liquid Vapor Phase Change Phenomena: An Introduction to the Thermophysics of Vaporization and Condensation Processes in Heat Transfer Equipment, 2nd Edition. New York: Taylor Francis Group, 2008.

Carver, C. et al, "Modeling and development of photoelectrochemical reactor for H_2 production," *International Journal of Hydrogen Energy* 30 (2011) 1-13

de Hulst, Van H.C. (Ed.) Light scattering by small particles. New York: John Wiley & Sons, 1957.

Heavens, O.S. Optical Properties of Thin Solid Films. New York: Dover Publications, 1991.

Howell, John, Robert Siegel and M. Pinar Mengüç. Thermal Radiation Heat Transfer. 5th Edition. New York: CRC Press, 2010.

Hübert, Thomas, Uwe Beck, Helga Kleike. "Amorphous and nanocrystalline $SrTiO_3$ thin films," *Journal of Non-Crystalline Solids* 196 (1996), 150-154.

Kelzenberg, Michael et al. "Enhanced absorption and carrier collection in Si wire arrays for photovoltaic applications," *Nature Materials* 9 (2010), 239-244.

Kosten, Emily, Emily Warren and Harry Atwater. "Ray optical light trapping in silicon microwires: exceeding the $2n^2$ intensity limit," *Optics Express* 19 (2011) 3316-3331.

Nelson, Jenny. The Physics of Solar Cells. London: Imperial Press, 2003.

Tsakalakos, L. et al. "Silicon nanowire solar cells," *Applied Physics Letters*, 233117 (2007) 1-3.

Yu et al. "Geometrical optics approximation of light scattering by large air bubbles", Particuology 6 (2008) 340-346.

Zohdi, T. I. "Modeling and simulation of the optical response rod-functionalized reflective surfaces," *Computational Mechanics*, 50 (2012) 257 - 268.